Paraglacial history and structure of the Moosfluh Landslide (1850–2016), Switzerland

Author(s):
Glueer, Franziska; Loew, Simon; Manconi, Andrea

Publication date:
2020-04-15

Permanent link:
https://doi.org/10.3929/ethz-b-000390987

Originally published in:
Geomorphology 355, https://doi.org/10.1016/j.geomorph.2019.02.021

Funding acknowledgement:
146593 - Paraglacial Rock Slope Mechanics (Phase II) (SNF)
172492 - Paraglacial Rock Slope Mechanics (Phase III) (SNF)

Paraglacial history and structure of the Moosfluh Landslide (1850-2016), Switzerland

Franziska Glueer[1], Simon Loew[1], Andrea Manconi[1]

[1]Department of Earth Sciences, Engineering Geology, ETH Zurich, Zurich, Switzerland

Abstract

Rock slopes next to the tongue of the Great Aletsch Glacier, Switzerland are characterized by rapid environmental adjustment to non-glacial conditions. This study investigates and describes in detail the historic development of the largest rock slope instability in this area, called Moosfluh Landslide. We study in detail the structure, evolution and stability since the end of the Little Ice Age (LIA) until September 2016 and discuss their relationships with the evolution of the Great Aletsch Glacier since the Lateglacial period. In 2016 around 50 m of glacial ice thickness were left at the Moosfluh Landslide toe, where in 1850 glacial ice was more than 400 m thick. The changing stability conditions at the interface with the melting valley glacier are studied based on novel balanced cross sections and kinematic model of the Moosfluh Landslide dominated by toppling phenomena in metamorphic rock. The morphology and evolution of this landslide since the LIA are investigated with multi-temporal landslide maps based on aerial digital photogrammetry (ADP) applied to historic images since 1961. Internal deformation at Moosfluh is accommodated by shear slip along uphill-facing foliation and fault planes, and by extensional faulting forming tension cracks and graben-structures at the landslide head. Together with Digital Image Correlation (DIC) and total station monitoring (TPS) the Moosfluh Landslide displacement history was reconstructed, evidencing post-Egesen landslide displacements and an acceleration of movements since the LIA and especially since 2007. The displacement rates increase from few mm per year until the nineties to several meter per day in September 2016. Different kinematic models have been tested and changes in the Moosfluh rock slope stability in response to retreating glacial ice and changing groundwater conditions was explored with limit-equilibrium analysis of the stepped planar block toppling model of Goodman and Bray (1976). For the observed conditions and a toppling joint friction angle of 19° the simulated factor of safety drops non-linearly from the LIA maximum (1.12) to the year 2007 (1.02), when the height of ice above the valley bottom melted down to 100 m.

This study illustrates with unprecedented detail the time scales, displacement magnitudes and structural evolutions of a large toppling mode slope instability in a paraglacial setting. The long-term cumulative slope displacements between the Egesen stadial and the LIA are of the same magnitude as the cumulative displacements between the LIA and the year 2016. As large portions of the studied slope underwent multiple retreats and advances of the Great Aletsch Glacier during the Lateglacial and Postglacial period, the observed onset of large slope displacements should be related to incremental damage (slip weakening and weathering) occurring along steeply dipping toppling fractures during the LIA.

1 Introduction

Large-scale rock slope failures, such as rock-avalanches, translational rock-slides and deep-seated gravitational slope deformations (DSGSD), are commonly found in formerly-glaciated alpine areas. According to existing literature DSGSD occur on high-relief hillslopes, often affect the entire slope, and show displacement relatively small compared to the slope itself (Agliardi et al., 2001).

A classical hypothesis from the 19th century directly relates failure in alpine landscapes to former glaciation and deglaciation (Heim, 1932; Abele, 1974; Evans and Clague, 1994; Ballantyne, 2002; Holm et al., 2004; Oppikofer et al., 2008; Strozzi et al., 2010; McColl and Davis, 2013; Coquin et al., 2015; Clayton et al., 2017). However, closer inspection of available data shows that the triggering events and causes of many paraglacial slope failures have remained elusive and the response of rock slopes to glaciation and deglaciation is variable and influenced by the combination of many different factors (McColl, 2012).

The determination of landslide age can lead to a better understanding of causes, frequency and recent and future responses of slope instabilities to climate change (Lang et al., 1999; Corominas and Moya, 2008; Ivy-Ochs et al., 2008; Huggel et al., 2012; Stoffel et al., 2014; Mercier et al., 2017). While some rock slopes show rapid reactions to recent and ongoing glacial retreats since the Little Ice Age (e.g. Oppikofer et al., 2008; Kos et al., 2016; Fey et al., 2017), numerous recently dated landslides in formerly glaciated mountains slopes show no direct reaction to glacial unloading (Cossart et al., 2008; Hippolyte et al., 2012). Typical lag times between glacial retreat and rock slope collapse are suggested to be in the order of hundreds to thousands of years (Bigot-Cormier et al., 2005; Dortch et al., 2009; Ivy-Ochs et al., 2009; Ballantyne et al., 2014; Mercier et al., 2017).

The potential occurrence of rock slope instabilities is controlled by preconditioning factors such as lithology, faulting, bedding and slope orientation. If these factors are unfavorable to stability, preparatory factors (long term) and triggering factors (short term) can result in slope movements and eventually to slope failures. Preparatory factors include glacial erosion, sheet jointing, static fatigue or weathering, and short term triggering factors include seismic events and exceptional pore pressure increases (Gunzburger et al., 2005; McColl, 2012; Ballantyne and Stone, 2013; Prager et al., 2008). The impacts of glacial erosion, steepening of valley sides and deglaciation processes on progressive rock strength degradation (also called damage) and deformation of adjacent rock slopes have only recently been subject of detailed mechanistic studies (e.g. McColl, 2012; Ballantyne et al., 2014; Ziegler et al., 2014; Leith et al., 2014; Grämiger et al., 2017, 2018; Oppikofer et al., 2017). In a paraglacial context, cyclic loading from daily, annual and interstadial climatic variations are additional preparatory factors only rarely discussed explicitly in literature so far (e.g. Grämiger et al., 2018). The removal of the support from adjacent glacier ice, called glacial debuttressing, was long considered to be a key factor generating large rock slope failures in deglaciated mountain ranges (Cruden and Hu, 1993; Ballantyne, 2002; Seijmonsbergen et al., 2005; Coquin et al. 2015; Mercier et al., 2017). However, recent studies pointed out that the glacial ice is not able to efficiently buttress an unstable slope at small strain rates due to ductile creep (McColl et al., 2010). In addition, high pore pressures below temperate valley glaciers reduce the ice loads of valley glaciers on the adjacent slopes. Despite a common belief that earthquakes, rapid snowmelt and rainfall events are the main triggers for large rock slope failures, absence of clearly observable triggering mechanisms appears to be very typical (Wieczorek and Jaeger, 1996), which presents a significant problem for hazard management.

In this study we present a comprehensive investigation of a large DSGSD at the Moosfluh slope, located at the current tongue of the Great Aletsch Glacier, the largest glacier in the European Alps (Figure 1). This slope fits all diagnostic features of a DSGSD as listed in Agliardi et al. (2001) with a high relief-energy hillslope, typical morpho-structures like ridge top depressions, numerous uphill-facing scarps and low displacement rates. The accessibility of this site and the available data sets relevant for reconstructing glacial and rock slope history and their mechanical interaction are unique. In addition Grämiger et al. (2017) have compiled a unique reconstruction of glacier fluctuations during the Lateglacial and Holocene period and studied long-term responses of the adjacent slopes through numerical modeling. In this paper we investigate the structures and responses of the Moosfluh rock slope instability to the retreat of the Great Aletsch Glacier since the Lateglacial period, with main focus on the last 150 years (i.e. the time since the Little Ice Age, LIA).

We use multiple methods to reconstruct the detailed displacement history of this DSGSD and relate it to the bedrock structures, the kinematics of the landslide body, the surrounding rock mass, the glacier extent and thickness, as well as the hydro-mechanical driving factors. Multi-temporal stereo-photogrammetric analysis of historic aerial photographs (ADP) since 1961 allows landslide mapping at a time where the Great Aletsch Glacier held more than 280 m in ice thickness above the toe of the Moosfluh DSGSD. Data from satellite positioning with global navigation satellite systems (GNSS; Lambiel and Delaloye, 2004; Glabsch et al., 2009) as well as terrestrial and satellite differential radar interferometry (D-InSAR; Massonnet and Feigl, 1998; Tarchi et al., 2003; Strozzi et al., 2003; Delacourt et al., 2007) are other data sets used for comparison of surface displacements between 1992 to 2016 (Strozzi et al., 2010, Kos et al., 2016). The main technique used in our study to monitor surface displacements are measurements conducted by robotic total stations (TPS). A large set of high-accuracy three-dimensional topographic measurements capture ground surface displacements at high spatial and temporal resolution since 2013. Together with data from Digital Image Correlation (DIC) of ortho-images from 2005-2016, point displacement monitoring (TPS) from 2011-2016 and field mapping, geomorphic zones within the landslide could be identified. Figure 2 shows the available data for the reconstruction of the history and structure of the Moosfluh Landslide for this study.

In this paper we analyze the behavior of the Moosfluh Landslide up to September 2016. After this time, this instability underwent a rapid acceleration (referred to here as the Moosfluh Crisis) which will be presented and analyzed in a future paper.

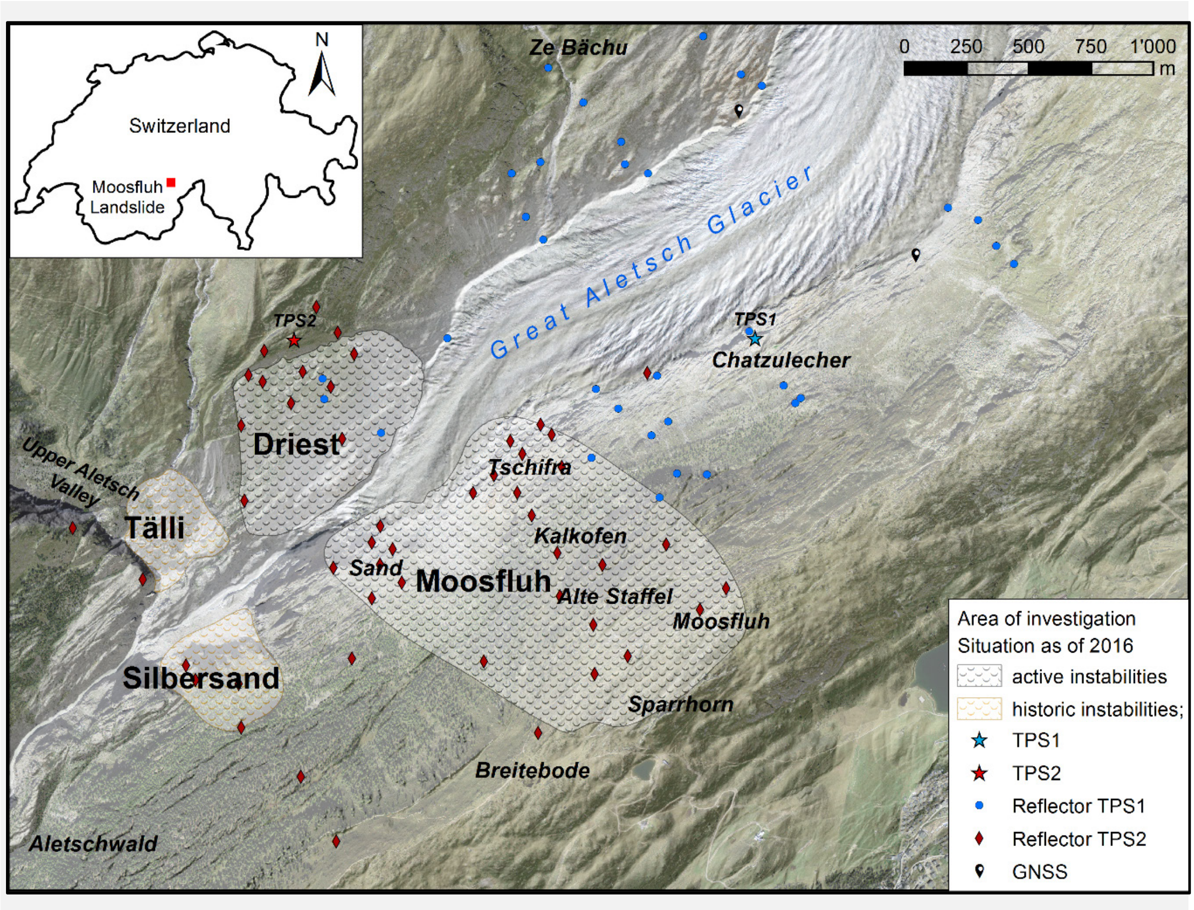

Figure 1. Area of investigation at the Great Aletsch Glacier (Valais, Switzerland) with the monitoring network installed at the glacier tongue as of 2016 consisting of two Total Stations, automated GNSS stations, reflectors in stable ground and reflectors within the perimeter of two historical (Tälli and Silbersand) and two recent landslides (Driest and Moosfluh). Approximate landslide boundaries based on Steck (2011) and own investigations.

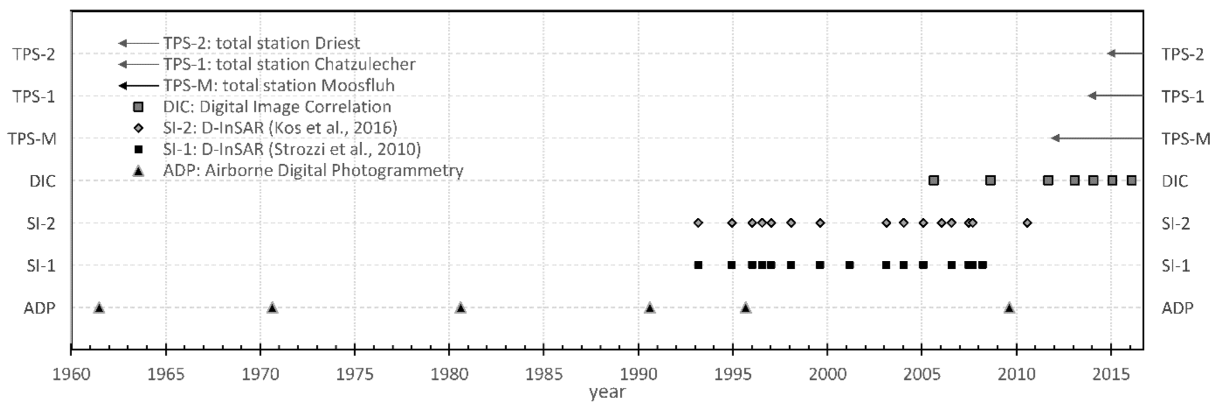

Figure 2. Data-sets available during this study to analyze the evolution of the Moosfluh slope instability.

2 Study site

2.1 Geology

Bedrock of the study area (Figure 3) belongs to the Southern Aar-Massif, which is characterized by several types of gneiss (pre-Variscan basement rocks) and late Variscan intrusive rocks of the central Aar Granite sequence. The lithologies include high-grade metamorphic rocks such as Augen-Gneiss, Biotite-Plagioclase-Gneiss, migmatites, serpentinite and magmatic rocks such as Central Aar-Granite, diorites, pegmatites, aplites, rhyolites and lamprophyres (Huttenlocher, 1933). The rock mass of the Aar-Massif was deformed by the Tertiary Alpine deformation and folded and thrusted in NW direction (Steck, 1968a; Steck and Hunziker, 1994). The alpine deformation created not only a strong foliation but also ductile to brittle shear zones within the study area (Labhart, 1965; Steck, 1968b).

The gneissic layering is well defined with a steep to sub-vertical dip towards SE, which leads to a strike direction of discontinuities parallel to the flanks of the valley at the glacier tongue. On the valley slopes SE of the glacier the foliation dips into the slope. Furrer (1948) recognized different types of foliation parallel structures that dip 70-90° towards the SE: Whereas the sericitic Augen-Gneisses as well as the igneous intrusions retained a massive fabric, the schistose and mica-rich sections show strong, deep weathering and crush zones.

2.2 Rock mass characterization

In order to characterize the rock mass at the Moosfluh Landslide and its surroundings, field parameters were collected for joint properties including dip direction/dip, spacing and persistence. These data was combined with data from previous studies about Schmidt hammer rebound hardness and Joint Roughness Coefficient (JRC; Grämiger et al., 2017). The results of this structural analysis are summarized in Figure 3. Three main joint types and sets were observed with the following average properties:

- F1 dips steeply to sub-vertically towards SE (dip direction/dip: 137/77). This very closely (cm) to extremely widely spaced (>6 m) and highly persistent joint set (trace length of 10-20 m) is the most abundant one in the area and correlates with the Alpine foliation in the Aar Massif (Steck, 2011). Schmidt hammer rebound harness is in the range of 48±10 and the JRC is 6±3. This set is characterized by unweathered as well as extremely weathered zones.
- F2 dips very steeply to sub-vertically towards SW (204/83). This fracture set is of low persistence (1 – 3 m) and widely spaced (0.6 – 2 m). Schmidt hammer rebound harness is in the range of 52±11 and the JRC is 6±3. There are 1-10 mm apertures, sometimes infillings and often only slightly weathered fracture surfaces.
- F3 dips gently NW with an average of (320/20), although orientation varies strongly. Joint set F3 is medium persistent (3 – 10 m) and very widely spaced (2 – 6 m). Schmidt hammer

rebound harness is in the range of 51±5 and the JRC is 7±4. F3 is accompanied and often represented by exfoliation joints.

These main sets match the schistosity, and J1/J2 fracture sets mapped by Kos et al. (2016). The rock mass is generally blocky, undisturbed and with good surface conditions (GSI 65-80). Weak planar structural planes are represented along folation (F1) and will dominate the rock mass behavior. The surface quality of the very closely spaced F1-discontinuities can be very poor with highly weathered surfaces and a weak schistose structure representing a GSI within these layers of only 5-25. These strongly sheared and incompetent mica schist layers rarely contain fault gouge (Figure 5b) and are often correlated with strong internal foliation and fracturing.

2.3 Glacial history

The Lateglacial and Holocene glacier extents in the Aletsch region have been studied by Holzhauser (1995), Kelly et al. (2004) and Jouvet et al. (2011). Dated Lateglacial moraines (Egesen), Little Ice Age (LIA) maxima and retreat stages are clearly visible or documented along the slopes bounding the Great Aletsch Glacier (Figure 3). The first major Pleistocene glaciation (~0.9 Ma) in the Alps presumably carved the deep trough form of major Alpine valleys (Muttoni et al., 2003; Haeuselmann et al., 2007; Leith et al., 2014) and several glacial cycles have since reworked the trough morphology. After the ice-free interglacial called Eemian (~130 to 115 ka; Dahl-Jensen et al., 2013) in which the Aletsch region most likely was completely ice-free, the late Pleistocene hosted the Wuerm glacial period which lasted ~100 ky and peaked in the Last Glacial Maximum (LGM) dated at ~28 ky to ~18 ky (Ivy-Ochs et al., 2008; Ivy-Ochs et al., 2015). During this time the Aletsch Glacier region was a large icefield reaching into the Rhone Valley and covering the whole Moosfluh ridge under ice. Bedrock striations and a rounded surface of the ridge are evidence of this glacial overburden. After the LGM the ice retreated strongly and a series of successive glacial readvances occurred (Gschnitz, Clavadel, Daun, Egesen; Maisch et al., 1999; Ivy-Ochs et al., 2008; Darnault et al., 2012). Moraines of the last Wurmian readvance (Egesen) are well preserved in the Moosfluh area and cosmogenic exposure ages coincide with the Younger Dryas cold period (~12 ky BP, Alley et al., 1993; Kelly et al., 2004; Schindelwig et al., 2012). During the subsequent Holocene the Aletsch Glacier has retreated considerably, interrupted by several readvances culminating in the Little Ice Age (LIA) around 1850 (Joerin et al., 2006; Ivy-Ochs et al., 2009; Nicolussi and Schlüchter, 2012; Schimmelpfennig et al., 2012), when the Aletsch glacier was more than three kilometers longer and 300 m thicker than today (Glaciological reports, 1881-2017). Glacial retreat is ongoing at the Aletsch Glacier and shows a vertical glacier loss in the area of the Moosfluh Landslide between the end of LIA (1850) and 2016 of approximately 320 m at Cross Section A, 350 m at Cross Section B, and 380 m at Cross Section C, where in 2016 complete ice free conditions are found (for location see Figure 3), resulting in ice downwasting of more than 2 m/a and a loss of 3.1 km in length.

By radiocarbon dating of fossil tree trunks overrun by advancing ice and later being exposed during retreat, Late Holocene glacier fluctuations could be reconstructed in detail (past ~3500 a, Holzhauser et al., 2005). The extent of the LIA is not always clearly visible in the field today since this extent may have been reached several times before, generating compound moraines (Schimmelpfennig et al., 2012). Holzhauser et al. (2005) believes that the Great Aletsch Glacier during Bronze Age Optimum (3350-3250 a ago) was still about 600 m shorter than today. The bedrock above and outside of the LIA extents most likely experienced only one single glacier readvance (Egesen stadial) following LGM ice retreat, whereas rock slopes within and below the LIA extent were affected by several glacial loading cycles (Grämiger et al., 2017).

2.4 Rockslide overview

A concentration of rock slope instabilities has been mapped in the study area (Figure 1):

- (1) The Tälli landslide, which is located at the intersection of the Upper Aletsch Valley and the Great Aletsch Glacier, covers an affected failure surface area of around 124,000 m². Historic aerial images show that Tälli started to build a visible main head scarp in 1966, developed a lateral release area and collapsed in 1970 - at a time when the Great Aletsch Glacier just retreated from the toe of the landslide.
- (2) The Driest landslide with its distinctive white band of freshly exposed rock at the bottom of the main head scarp. Total station monitoring data from 2014 to 2016 show displacement rates of ~30 mm/a and an affected surface area of 420,000 m². The initiation age of the Driest slope movement is estimated to 7.4 ky before present as constrained by ^{10}Be dating (Grämiger et al., 2017).
- (3) The historic Silbersand landslide, which is characterized by its relict 30 m high head scarp. This currently stable mass was active at least 150 years ago since the LIA lateral moraine accumulated in situ on top of the displaced mass. Glacial erosion features along the scarp indicate post-Egesen/pre-LIA age, however current TPS monitoring reveals a stable state of the 160,000 m² affected surface area of the landslide.
- (4) The Moosfluh Landslide, which is the main topic of this study, is the largest mass movement (affected surface area: 1’320,000 m²) of the region around the glacial tongue in the southeastern valley flank. It is partly covered by the Aletsch Forest, and has been described previously as a toppling-mode landslide by several authors (Strozzi et al., 2010; Loew et al., 2017; Kos et al., 2016).

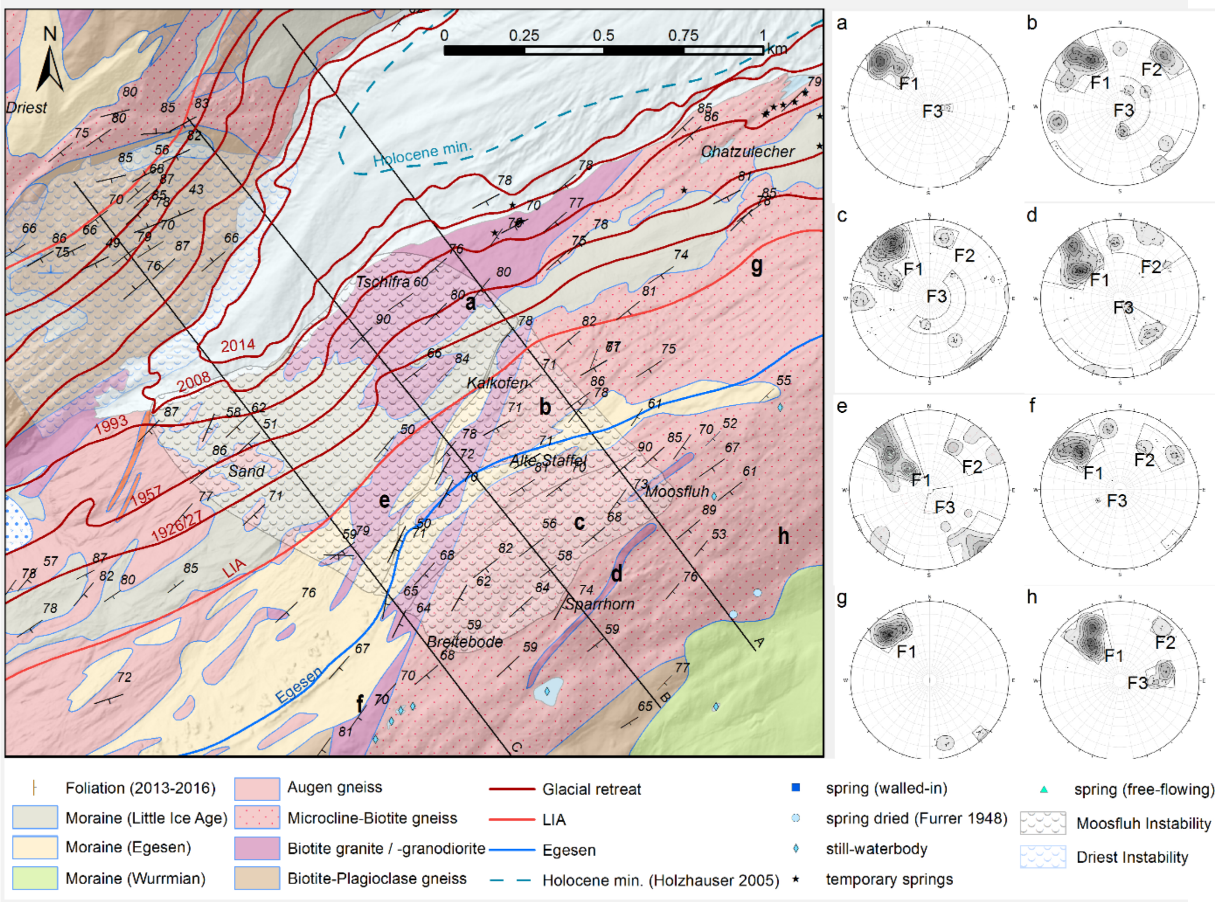

Figure 3. Glacial, geological, hydrological and structural setting of the Moosfluh area: Geology (Steck, 2011), field-mapped foliation (average dip of > 20 measurements indicated), stereoplots of joint sets within the area for labelled domains (a-h), glacial retreat between Egesen and 2014, elevation of Holocene glacial minimum (Holzhauser, 2005), field-mapped springs and water bodies, and the current extent of the Moosfluh Landslide.

3 Landslide morphological features

3.1 Methods and materials: Photogrammetric data acquisition and processing

Historical aerial photographs were used for Aerial Digital Photogrammetry (ADP) and 3D topography models were built from the years 1961, 1970, 1980, 1990, 1995 and 2009 as well as from 2012-2016. The first six sets of aerial photographs (1961-2009) were received from Swisstopo (Bundesamt für Landestopografie) and delivered with basic camera specifications like camera type, camera coordinates, image size, lens type, focal length and focal plane frames for the photographs. To achieve high accuracies a camera calibration for each photograph has been processed considering the camera parameters in 3DM CalibCam (Adam Technology, 2012).

To geospatially reference the models ten stable ground control points (GCP) with known coordinates in CH1903 LV03 and evenly distributed in the near stable surroundings of the Moosfluh instability were selected and identified within the historical photographs wherever possible. A summary of input photograph characteristics and resulting model parameters is provided in Table 1. The calibrated photographs were combined into a 3D stereo model in 3DM Analyst (Adam Technology, 2012), where orthorectified epipolar images act as a base for high-density Digital Terrain Models (DTM) generation. Based on the standards proposed by the Geological Society of London for geomorphological mapping (Arguile et al., 1982) geomorphological analysis and interpretation have been applied to the Moosfluh Landslide documenting slope geometry from 1961 to 2016.

Table 1. Summary of photogrammetric model generation parameters.

Image Info			Photogrammetry Info				
Date	Camera Type & Lense	Image Size (px)	Control Point Accuracy (m; x,y,z)	Image accuracy (px)	Total RMS (m)	Point Density (pts/m²)	Number of GCP
1961-07-26	RC5 29 11.5 AG	9478 x 8954	0.1, 0.15, 0.17	0.18	0.25	7	6
1970-09-21	RC5 15 UAg	16831 x 17765	0.05, 0.09, 0.17	0.28	0.2	32	6
1980-09-04	RC10 UAg II 3008	16828 x 16776	0.07, 0.09, 0.13	0.15	0.34	12	7
1990-09-06	RC10 15/4 UAg	16766 x 16809	0.07, 0.06, 0.13	0.18	0.16	29	7
1995-10-02	RC30 15/4 UAg-S	16860 x 16859	0.03, 0.04, 0.06	0.17	0.08	25	5
2009-09-08	RC30 15/4 UAg-S	16646 x 17002	0.08, 0.12, 0.20	0.19	0.25	7	6

3.2 Results: Geomorphological analysis

The existing high quality aerial photographs allow for detailed analysis and comparison of features within the landslide and its surroundings. DTMs produced from Aerial Digital Photogrammetry (ADP) as well as derived raster maps of slope dip, slope aspect and hillshade representation of topography were used to identify abrupt or gradual steepening or shallowing of the slope, gullies, ridges, cliffs and temporal changes in morphology. A map of the morphometric features of 2009 is presented in Figure 4 and 5a. The large scale morphology of the Moosfluh Landslide area can be subdivided into three Sectors: from the undulating plain at the Moosfluh ridge the slope dips with 25° degrees to the plane of Alte Staffel (Sector I), then dips with 37° to the plane of Kalkofen (Sector II) and finally dips with >39° to the current Aletsch Glacier elevation (Sector III). It is important to note that the flattened areas (or shoulders) of Kalkofen and Alte Staffel are only developed within the Moosfluh Landslide. The plain of Moosfluh in Sector I with its small moors and swamps is interpreted as a wide extensional horst and graben structure with slope parallel uphill- and downhill-facing faults (Figure 5e) limited by the large head scarp of the Sparrhorn cliffs facing towards the NW (Figure 5f). This has been interpreted in a similar way by Strozzi et al. (2010) and Kos et al. (2016). The oversteepened toe of the Moosfluh Landslide is characterized by many uphill-facing scarps with trace length of about 100 m not only below Kalkofen at Tschifra but also around Sand, where a secondary landslide developed in 2015. A detailed description of geomorphic features can be found in Supplementary Materials A.

Convex and concave slope breaks and changes, cliffs, ridges, depressions and glacial ice and slope directions have been systematically mapped on the historical photograph of 1940, and on the DTM's of 1961, 1990 and 2009 (Figures 4 and 5a). The Moosfluh Landslide contains many slope parallel paired depressions and ridges forming very narrow (5-20 m) and long (100-1000 m) asymmetric graben structures visible both within exposed bedrock and in areas covered by a blanket of surficial soil (Figure 5d). The primary origin of these features could be glacial erosion, as they often follow weak schist and cataclasites (Figure 5b), oriented parallel to the strike of the steeply dipping regional foliation (approximately SW-NE). Furrer (1948) describes this phenomenon as mainly caused by the strong weatherability of mica schist and crushing zones within the gneisses. Kos et al. (2016) interpret most of these structures as up-hill facing scarps. This would imply that the Moosfluh landslide had a much larger lateral extent in the geological past. Ambrosi and Crosta (2006) reported that many scarps and uphill-facing scarps in alpine environments are a result of gravitational phenomena rather than of neotectonics and seismic activity. At Moosfluh the meter-scale asymmetric grabens seem to be an older product of gravitational deformation along phyllosilicate-rich layers combined with glacial erosion. These morphologic forms with orientation always parallel to bedrock foliation can be found in the whole area of pre-Variscan basement rocks within the Aar-massif between Bettmerhorn to Gibidum and on both slopes besides the Great Aletsch Glacier.

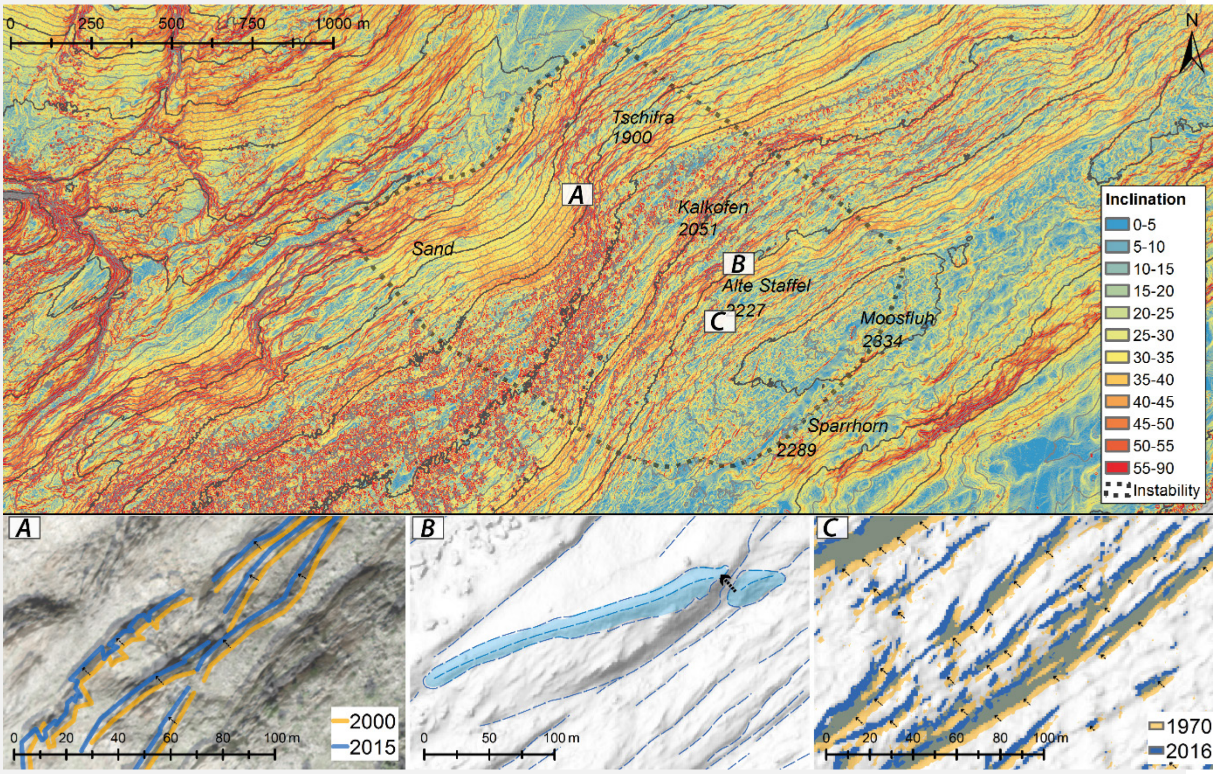

Figure 4. Analysis of slope morphology based on DTMs, hillshade, slope aspect, slope exposition and aerial ortho-images derived from Aerial Digital Photogrammetry (ADP) of the years 1961 to 2016. Location A (646099/138967): Displacements of traced cliff lines mapped on aerial ortho-images from 2000 and 2015. Location B (646679/138631): The Egesen lateral moraine outlined on the hillshade of 2016 is cut and displaced by several metres by an uphill-facing scarp; Location C (646688/138523): Displacements of NE-SW trending paired linear depressions parallel to foliation on the NW facing Moosfluh slope of 2016 (blue) overlaid by the same structures of 1970 (orange).

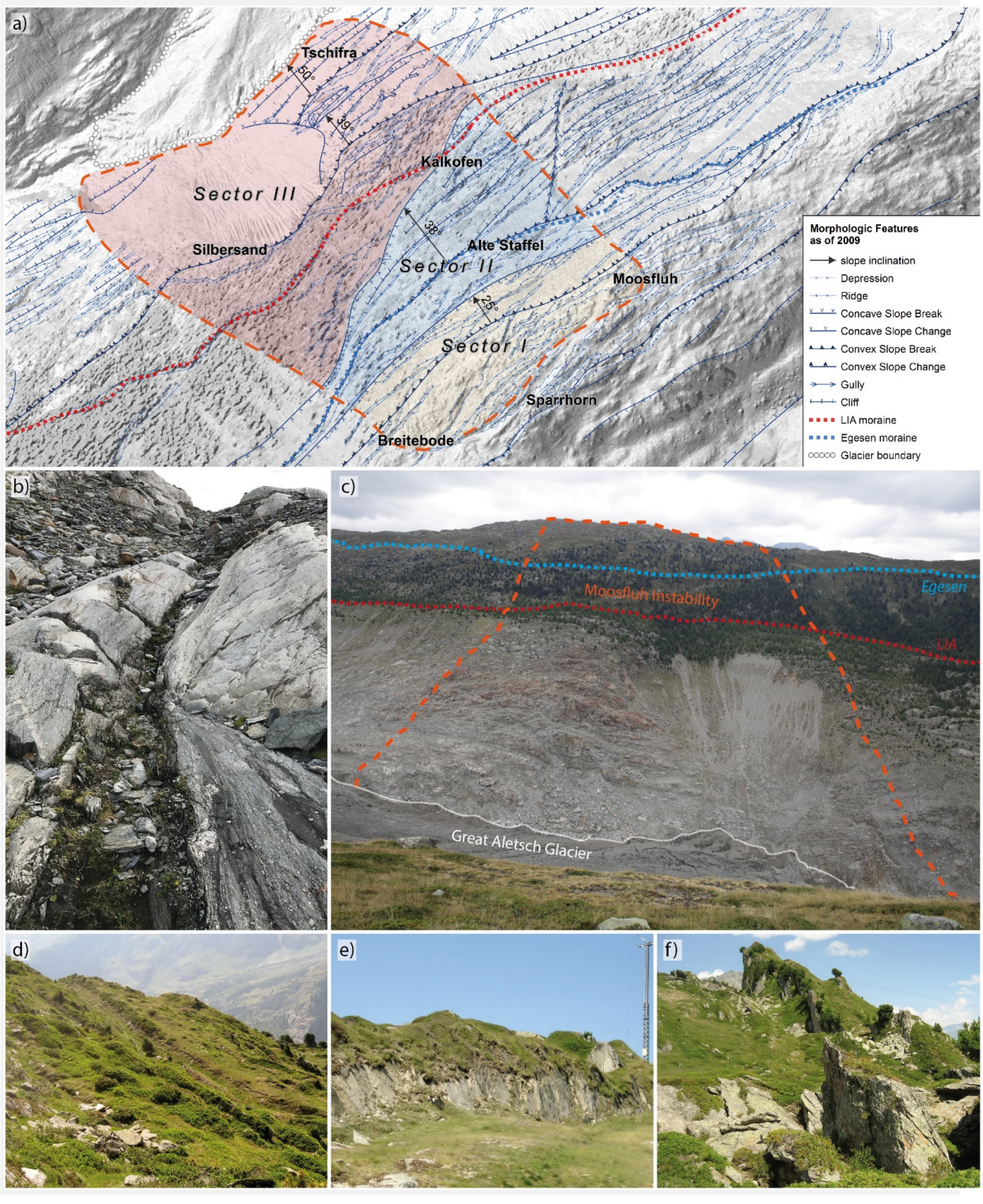

Figure 5. Morphology of the Moosfluh Landslide with (a) map of 2009 showing the large- and small-scale morphologic features based on aerial photographs and 3D photogrammetric analysis. (b) Combination of erosion and historic gravitational deformation along weaker mica-schist layers as bands of several dm widths. (c) View of the Moosfluh Landslide from the other side of the slope in 2015 with Egesen and LIA moraine/trimlines and current extent of the instability and glacier in 2015. (d) Slope parallel trenches and ditches with picture view looking downslope towards the plane of Alte Staffel. (e) At the undulating plain of Moosfluh looking towards the construction site of the Moosfluh cable car in 2015 a downhill-facing scarp of about 1 m

height and several tens of m length. (f) The Sparrhorn cliffs with up to 30 m height serving as head scarp of the Moosfluh Landslide.

Historical photographs recorded since 1940 document freshly exposed bedrock (by recent glacial retreat) showing the same slope parallel morphostructures as the slope further uphill and long uncovered from ice: Ridges and depressions ranging in elevation from 10 to 18 m running slope-parallel for 30 m to 1000 m throughout the entire slope (Figure 5a). No offset of these structures is evident at the current lateral borders of the landslide. The slope parallel depressions crossing the Moosfluh ridge are locally filled with morainic material, which suggests pre-Egesen origin of these depressions. On the other hand and in contrast to Strozzi et al. (2010), at Alte Staffel the Egesen moraine is cut and separated by a slope-parallel depression and continues with an offset of few m further downslope (Figure 4B and Figure 6). This suggests that some of the weaker mica schist layers forming slope parallel depressions have been gravitationally activated in extension after the Egesen stadial. At the slope below the Moosfluh ridge the NE-SW trending paired linear depressions parallel to foliation show a systematic downslope movement and a lateral growth on aerial ortho-images taken between 1970 and 2016 (Figure 4C). At the same time, at the slope toe near Tschifra, all cliff lines mapped on aerial ortho-images from 2000 and 2015 within the Moosfluh extents show downslope displacement of a few m (Figure 4A).

The lateral moraines of the Egesen and LIA stages are well preserved along the Southern valley slope (Figure 5a, c and 6) and only short parts are missing or not well preserved in the region of the Moosfluh Landslide. Already Kos et a. (2016) and Grämiger et al (2017) have noted horizontal displacements of the Egesen moraine within the Mossfluh landslide body. By tracing the horizontal and vertical position of these lateral moraines along the hillslope we investigate potential cumulative displacements caused by gravitational slope movements at Moosfluh after the Egesen stadial. Figure 6b shows the elevation of the lateral moraines as a function of horizontal distance measured along the moraine, which suggests that the elevation of the Egesen moraine becomes progressively and significantly depressed in the western part of the Moosfluh. The amount of potential subsidence for the LIA lateral moraine is smaller than for the Egesen lateral moraine (about 50% of the Egesen moraine depression), and close to the range of natural elevation variations. The maximum cumulative (absolute) displacement magnitudes recorded in the central part of the Moosfluh instability in the period of 1850-1992 is 1.4 m (where displacements have been around 1 cm/a), from 1992-2007 in the range of 0.75 m and from 2007-2016 in the range of 4.6 m (Figure 9a). Altogether this results in a maximum cumulative displacement of little less than 7 m for the period 1850-2016.

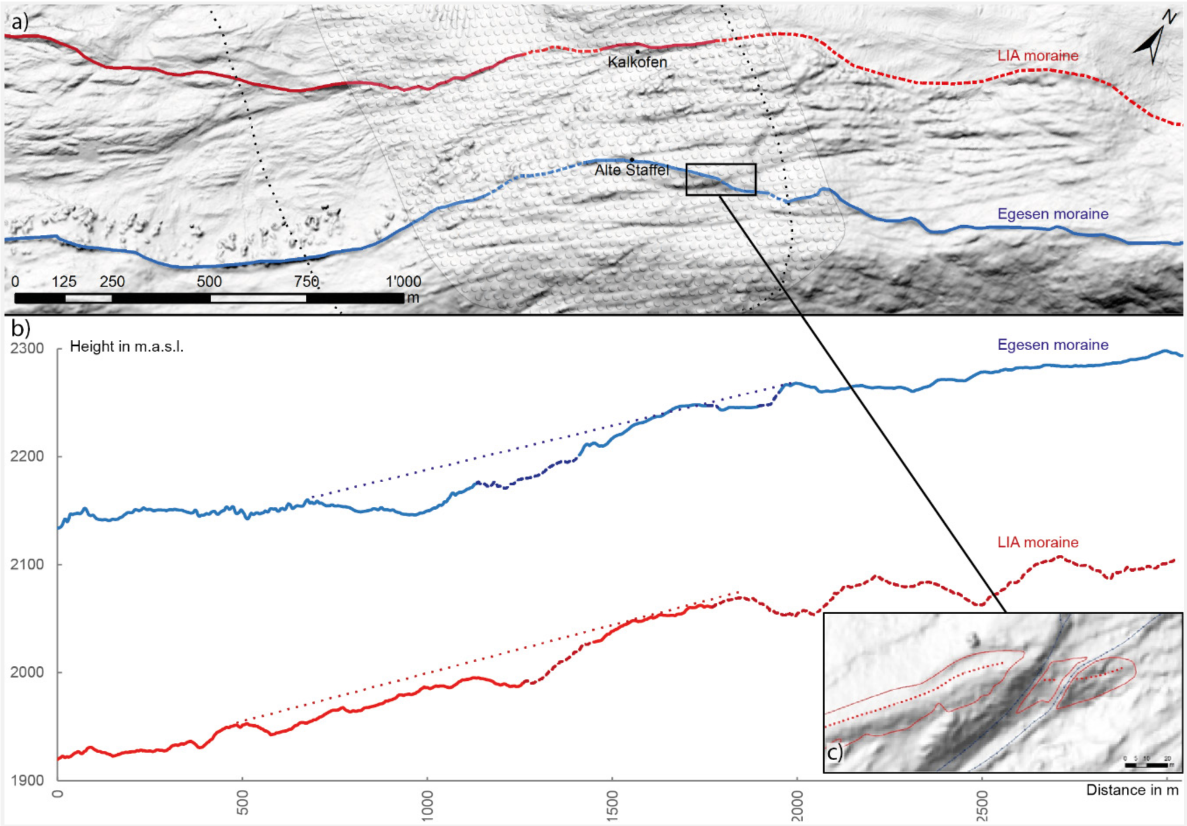

Figure 6. Landslide displacement history reconstruction. a) Map view with hillshade and contour lines of the Moosfluh Landslide area (swissALTI3D 2014) marked with the current extent of the Moosfluh Landslide (patterned), the possible historical extent (dotted black lines), Egesen lateral moraine and trimline (blue and dashed blue) and LIA (red and dashed red). b) Section view of traced Egesen and LIA lateral moraines along the slope showing an increasing downslope displacement at the area of Moosfluh Landslide for both moraines deviating from the expected in-situ moraine location (dotted red and dotted blue) and protracted on the NW' lateral border. c) Detail of Egesen Moraine being cut by an uphill-facing scarp and showing a downslope displacement of ~8-10 m.

4 Recent landslide displacement history

At the Moosfluh Landslide a 75-year record of slope morphology and displacement history can be extracted from photogrammetric analysis of historic aerial imagery (1961-2016), Digital Image Correlation (DIC) of orthorectified images (2005-2016) and high resolution geodetic monitoring (2011-2016). Maximum slope displacement rates obtained from the different analysis techniques and glacial ice heights recorded at Cross Sections A-C between 1961 and 2016 are shown in Figure 9a and 9b.

4.1 Methods and materials: Geodetic measurements and Digital Image Correlation

Since 1977 there is a skiing lift connecting Riederalp with the Moosfluh crest on the opposite slope side of the Moosfluh Landslide. The top station Moosfluh (2334 mn a.s.l.) lies inside but on the border of the instable landslide mass. There was a breakage of the lift in 1996 and in 2015 the entire lift was rebuild to adjust for movements of the top station. Therefore from 2011 onwards surveyors have monitored the surroundings of the Moosfluh cable car with a geodetic network once or twice per year (Planax AG, Visp). These data are integrated into the geodetic data set of this study which includes a comprehensive monitoring program of the entire area surrounding the lower part of the Great Aletsch Glacier, including both active instabilities as well as stable and marginally stable slopes (Loew et al., 2017). Figure 1 provides an overview of the location of all relevant measurement and monitoring sites located around the Moosfluh Landslide. Two total stations (TPS) and four permanent global navigation satellite system (GNSS) stations, two meteo-stations and more than 80 reflectors are employed in the surrounding rock slopes to detect and measure transient ground movements with mm-accuracy and at an hourly schedule since 2013. The currently monitored area extends over more than 3.5 km along and 2 km across the Aletsch valley ranging from altitudes between 2300 and 1600 m a.s.l.

The geodetic monitoring system at Chatzulecher (TPS1) is based on a Leica TCP 1201 operated since fall 2013 and a Leica Nova TM 50 at Driest (TPS2) which was installed in 2014 to enlarge the system. The total stations are mounted on a double walled aluminum pillar to account for thermal deformation, unilateral temperature changes or vibrations. To report possible movements of the total station a GNSS sensor is located right above the total station and constantly taking its position (every 30 s). The total stations are housed in a protection shelter out of a polyamide cylinder with holes at the reflectors' location to allow for completely undisturbed measurements. Measurements are taken hourly throughout the night and in a 4 hour schedule during the day. Standard deviations of the resulting coordinates are 1 mm in horizontal and 2 mm in vertical direction for the GNSS data and +/- 1 mm for the TPS data. The extent of the network is constantly adapted to the changing conditions by installing additional reflector prisms in areas of interest. As of September 2016, 17 prisms have been placed inside the Moosfluh Landslide and another 18 prisms in marginally stable areas in the direct surroundings (Figure 7). More detailed information about the spatial distribution of landslide movement has been derived from Digital Image Correlation (DIC) analysis of orthorectified image pairs provided by Swisstopo (Figure 8). DIC aligns and registers two images of the same scene and measures the residual shift (internal deformation) by tracking the offset of common features. Only displacements occurring parallel to the camera axis can be measured. Depending on the area of study and the source imagery, DIC measurements can reach sub-pixel accuracies (Scambos et al., 1992; Delacourt et al., 2007; Manconi et al., 2018). In our specific case the pixel size of the ortho-images used in this study is 0.25 m and accuracies are in the range of ±0.1 m. Some DIC displacement maps are cut in the SE due to limitation in the earliest ortho-photo coverage.

4.2 Results: Landslide displacement evolution

3D displacement vectors are available for a total of ten reflectors at the Moosfluh slope from 2013 to 2016 and an additional seven reflectors at the ridge and behind the crest from 2011 to 2016. Mean 3D displacement vectors for the time period from 2011/11/18 to 2016/08/26 split in horizontal and vertical components of yearly intervals (in mm/a) are presented in Figure 7 and corresponding measurement data (3D displacement [mm/a], vector orientation [°] and plunge [°]) in Table 2. A detailed description of TPS measurement results can be found in Supplementary Materials B.

Averaged DIC displacements in the period 2005-2008 reach up to 0.1 m per year, with the highest displacements occurring in the SW corner of the landslide. Between 2008-2011 the maximum displacements do not increase beyond 0.1 m per year but i) the most active area shifts upstream the Aletsch valley and ii) maximum displacements stretch down to Kalkofen and beyond towards the glacier margin. From 2012-2013 to 2013-2014 this trend continues and the most active area moves up the valley and borders to the line Moosfluh – Alte Staffel – Kalkofen – Tschifra with a maximum width of about 700 m around Alte Staffel and a maximum displacement of 0.6 m/a in 2012-2013 and

0.7 m/a in 2013-2014 (Figure 8c and Figure 8d). In 2014-2015 the active area widens laterally on both sites whereas the landslide head area remains at a constant place. Maximum displacements are in the range of 0.8 – 1 m/a in 2014-2015 (Figure 8e) and increase to more than 1 m/a in 2015-2016 (Figure 8f). In 2015-2016 the movements in the headscarp area progress towards SE (50 m) and the most active sector (line from Moosfluh – Alte Staffel – Kalkofen – Tschifra) moves further upstream for another 30 – 80 m. Cumulative displacements from 2012-2016 clearly show the extent of the landslide and the most active area during this period (Figure 8b). When looking at the topographic map and the Digital Elevation Model (DEM) it can be seen that the most active area is mainly restricted to the wide ridge trending down from Alte Staffel to Kalkofen to the glacier margin at Tschifra, being elevated by around 50 m from the surrounding rock slopes (Figure 8a). Stacked DIC of ortho-images from 2012 – 2016 show clear lateral borders of the Moosfluh Landslide which are hard to observe in the field due to little displacement along the lateral margins and forested or soil covered surfaces (Figure 8b)

Results from DIC (Figure 8) and TPS measurements (Table 2 and Figure 7) fit quite well, e.g. for the highly active area around the Moosfluh ridge (around reflector 5004/36), and thus the DIC images show a representative horizontal displacement pattern for the Moosfluh Landslide area. DIC and TPS measurements throughout the years show an acceleration of movement along the entire slope from Tschifra to Moosfluh ridge. Tilts for the different reflectors stay more or less constant within the years (±5°) except for the SE lateral border where tilts vary >10°. Azimuths are all constant within 310° to 325° towards NW (see Table 2 and Figure 7). TPS-derived movement velocities until 2016 increase from the lateral margins towards the center of the instability and are highest at the top, diminishing downwards.

Figure 9a compiles all existing displacement data from this study with previously published D-InSAR displacements from Strozzi et al. (2010) and Kos et al. (2016). It can be clearly seen that the onset of accelerations towards the end of the last century corresponds to an increase in ice downwasting rate at the landslide toe. This confirms a previous correlation shown by Kos et al. (2016) between landslide velocity and ice height elevation change at the landslide toe. The delay in slope acceleration with respect to the ice downwasting rate, postulated by Kos et al. (2016), is not clearly visible in our new data set. The dramatic acceleration follows the classical power law function, superimposed by recharge variations during snow melt, and leads to annual velocities of 1m/a in 2016. Even higher velocities develop after September 2016 during the Moosfluh Crisis, and can be related to the formation and activation of planar sliding surfaces developing along toppling base surface (Glueer, 2019).

Table 2. Displacement data of selected reflector targets from 2011 to 2016 measured through geodetic monitoring from total station Driest (Reflector 30-36) with a Leica Nova TM50, total station Chatzulecher (Reflector 28, 29) with a Leica TCP 1201 and all other reflectors (5003, 5004, 5005, 1004, 109) from a local monitoring network referenced through GNSS-fix targets (Planax Visp).

	from 2011-11-18 to 2012-11-07			from 2012-11-07 to 2013-10-24			from 2013-08-21 to 2014-08-22			from 2014-08-22 to 2015-08-26			from 2015-08-26 to 2016-09-08		
Reflector	3D*	ori.*	plg.*	3D*	ori.*	plg.*	3D*	ori.*	plg.*	3D*	ori.*	plg.*	3D*	ori.*	plg.*
5003	59	350	-85	30	282	-80	57	289	-80	20	326	-60	10	281	-9
5004	486	316	-23	549	315	-18	690	315	-12	808	315	-18	1066	314	-17
5005	385	310	-35	431	310	-30	485	310	-19	576	311	-28	713	309	-26
1004	227	312	-35	251	315	-24	261	312	-6	312	315	-20	348	313	-17
109	191	313	-39	202	313	-27	201	313	-7	248	315	-21	265	313	-21
28	-	-	-	-	-	-	44	331	-26	119	323	-23	149	325	-25
29	-	-	-	-	-	-	68	325	-10	178	319	-13	221	320	-12
30	-	-	-	-	-	-	-	-	-	262	323	-10	458	323	-19
31	-	-	-	-	-	-	-	-	-	154	317	-15	359	323	-25
32	-	-	-	-	-	-	-	-	-	445	316	-13	878	316	-15
33	-	-	-	-	-	-	-	-	-	257	314	-20	536	319	-25
34	-	-	-	-	-	-	-	-	-	172	316	-14	438	316	-17
35	-	-	-	-	-	-	-	-	-	514	320	-21	1259	318	-23
36	-	-	-	-	-	-	-	-	-	675	310	-15	1450	311	-16

* 3D displacement in [mm/a], orientation from N in [°], plunge from horizontal in [°]

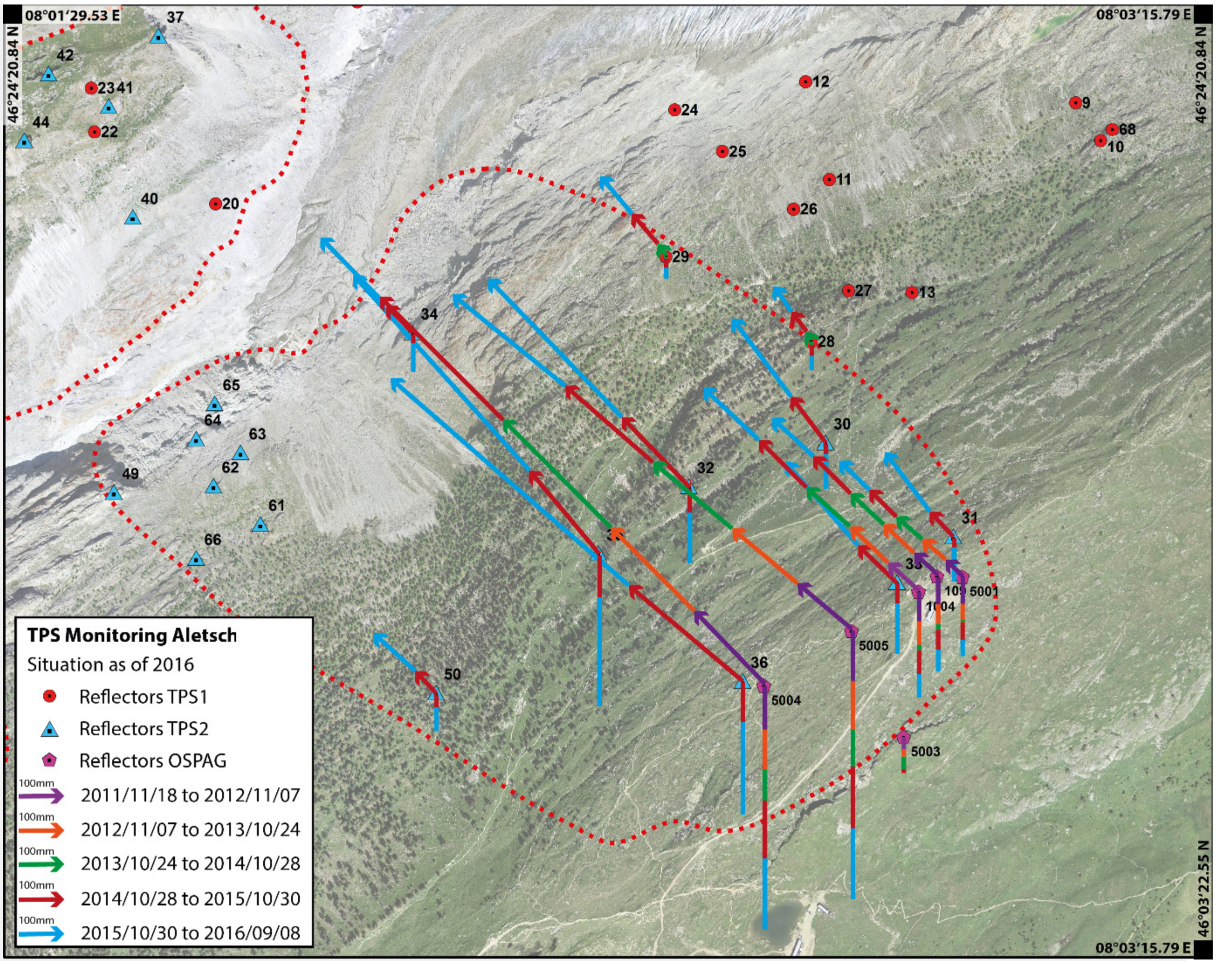

Figure 7. Scaled displacement vectors from the TPS monitoring network in horizontal (with arrow) and vertical (without arrow) components for yearly average displacements from 2011 to 2016. Maximum displacement rates in 2015/2016 can be found at

the ridge for reflector 36 (1.5 m/a), at Kalkofen for reflector 35 (1.3 m/a) and at the toe for reflector 34 with 0.4 m/a. Orthorectified image from 2016/09/08, approximate extent of Moosfluh Landslide in dashed red line as of summer 2016.

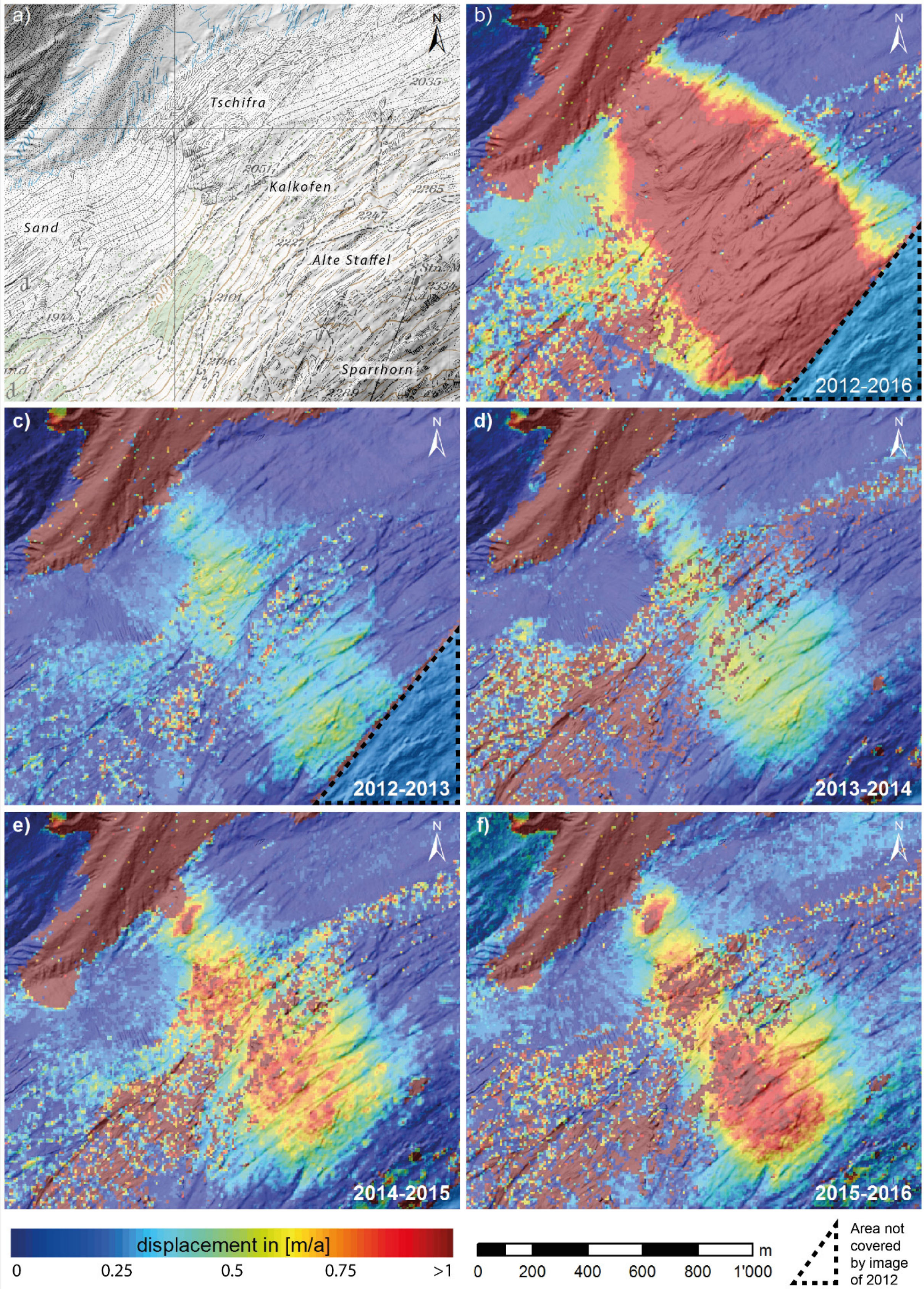

Figure 8. Digital Image Correlation (DIC) of orthorectified image pairs showing annual horizontal surface displacements for different years. a) Topographic map of the Moosfluh area with the oversteepened toe area at Tschifra, depression at

Silbersand, and plateaus of Kalkofen, Alte Staffel and Sparrhorn. b) Displacements between 2012/08/27 – 2016/08/26. c) Displacements between 2012/08/28 – 2013/08/21. d) Displacements between 2013/08/21 – 2014/08/22. e) Displacements between 2014/08/22 – 2015/08/26. f) Displacements between 2015/08/26 – 2016/08/26.

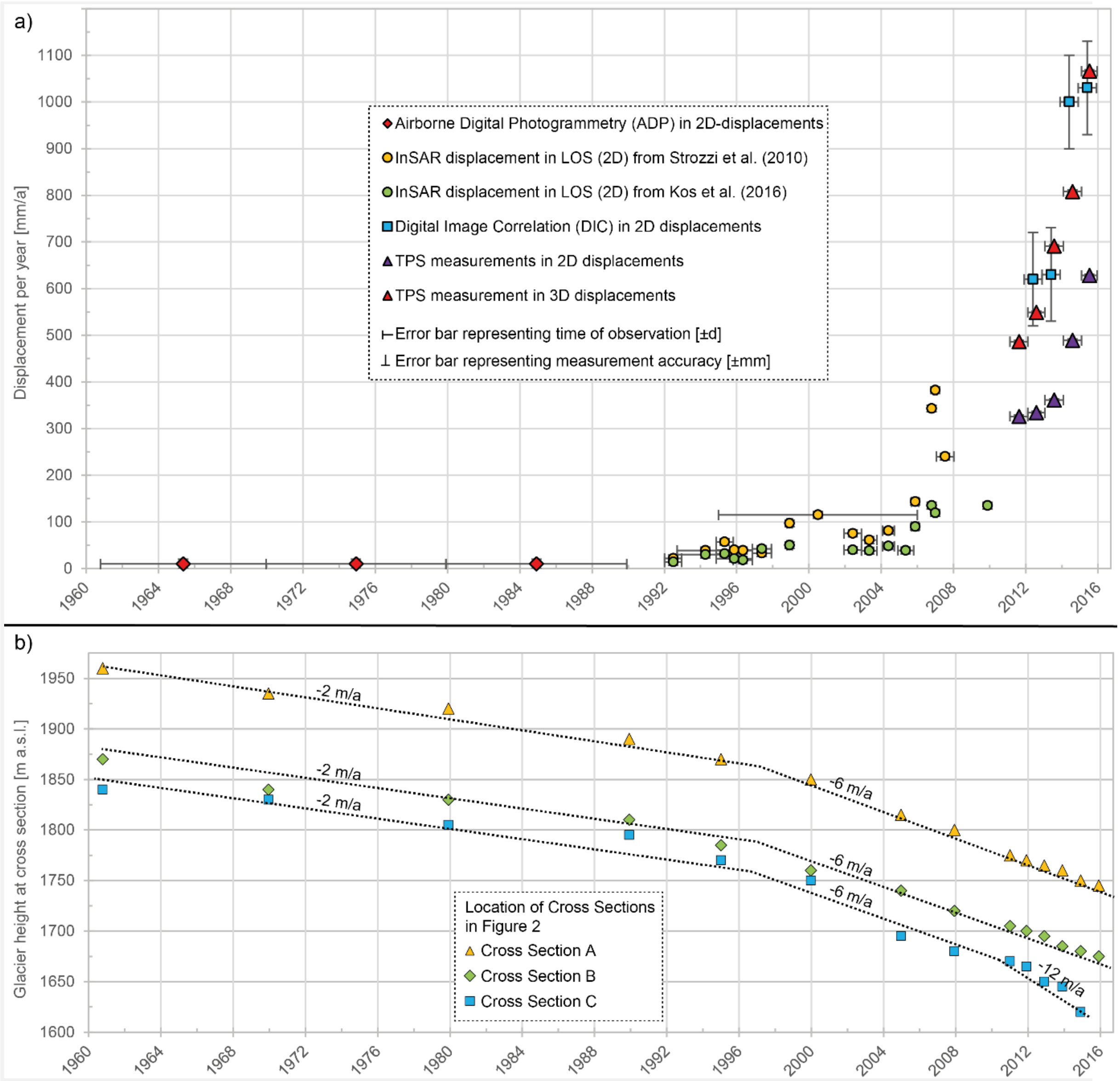

Figure 9. Moosfluh Landslide movement and glacial retreat (1960-2016) a) Maximum yearly displacement rates in 2D or 3D depending on data source from 1961 – 2016 at the upper slope (Sector I) of the Moosfluh Landslide with Aeerial Digital Photogrammetry (ADP) of historic photographs, D-InSAR displacements in Line of Sight (LOS) from Strozzi et al. (2010) and Kos et al. (2016), Digital Image Correlation (DIC) and Total Station monitoring (TPS) in LOS similar to D-InSAR data and in absolute 3D displacements; b) Recorded glacier heights at Cross Sections A-C located in Figure 3 in m a.s.l for the same period of time.

5 Landslide kinematics and structure

5.1 Methods and Materials: Stereographic analyses techniques

To understand the kinematics of the Moosfluh Landslide movements until September 2016, limit equilibrium and stereographic analysis techniques have been applied to structural data collected in the field. Usually the scale of the rock slope limits the application of this method to smaller rock slopes where the persistence of joints is of sufficient size (Stead & Eberhardt, 2013). For the large-scale slope movement of Moosfluh it is nevertheless applicable since the foliation-parallel fracture set is well developed and of persistent nature. Assuming rigid blocks, no cohesion, dry and fully persistent discontinuities, the stereographic method applied simply indicates the kinematically feasible modes for given slope and joint set angles. Key properties for analyzing toppling, sliding and wedge sliding in stereographic projection are the slope orientation, the dip angle of discontinuities and their friction angles (Wyllie and Mah, 2004).

As a first geometric constraint for toppling, the ratio of the base length Δx to the height y of individual blocks has to lie below the tangent of the dip angle (Goodman and Bray, 1976).In other words the block has to be high enough so that its weight can act through the block's lower corner to overturn and topple ($\Delta x/y > \tan \alpha$; Figure 10c). In a toppling rock slope also contacting columns and flexural slip of blocks occur. For such an interlayer slip to occur, the slope angle θ must be steeper than the friction angle φ plus the discontinuity normal γ ($\theta > \varphi + \gamma$; Goodman and Bray, 1976; Figure 10b). Additionally the azimuth between the steeply dipping discontinuities controlling toppling and the slope azimuth should be less than 30°, otherwise lateral fixation prevents toppling (Goodman, 1989).

For frictional sliding to occur at a block basal failure plane, a horizontal deviation from the slope dip direction (lateral limit) of 20° was considered (Wyllie and Mah, 2004). If the intersection line of two fracture planes plunges at an angle lower than the slope angle and greater than the friction angle, wedge sliding is possible (Markland, 1972). If the wedge is highly asymmetric, sliding along one of the two intersection planes occurs. This can be defined if the dip direction of this plane lies between the trend of the intersection line and the dip direction of the slope (Hocking, 1974).

5.2 Results: Slope kinematics and structural model

5.2.1 Slope kinematics

For the Moosfluh Landslide toppling, planar sliding and wedge sliding were analyzed with joint friction angles of 20° - 30° (Figure 11). Analyses were conducted for different slope inclinations, ranging from 315°/25° to 315°/75°. 315°/29° represents the mean slope exposition and inclination of the northwest exposed slope averaged over the whole Moosfluh slope. The mean slope orientation of Sector I is 315°/25°, of Sector II is 315°/38° and of Sector III is 315°/39° (for sectors see Figure 5). For the analysis of local (i.e. shallow) slope failures also steep rock walls with inclination angles of around 75° have been considered, these occur at Tschifra and below Alte Staffel and range from 5 m to 50 m in height.

Assuming standard friction angles and fracture orientations measured within the extents of the Moosfluh Landslide, toppling of F1 discontinuities was found to be the only kinematically feasible mechanism (dark red Figure 11). For an assumed friction angle of 30°, sliding along F3 becomes possible only for slope angles above 30°. The dip of F1 discontinuities (foliation) ranges from 90° to 56° with a weighted average of 80°. Assuming toppling joints with a friction angle of 30°, the lowest measured discontinuity dip (56°) requires a slope steeper than 64° (Figure 10b), i.e. this type of toppling is only possible as a local and shallow phenomena near steep rock walls. On the other hand for the average dip of 80° already a 40° steep slope is prone for toppling (respecting all other constraints mentioned above). Since foliation varies broadly within the study area, it can be concluded that for toppling to occur in Sector III (315°/39°) foliation must be between 90°-81° and for Sector II (315°/38°) between 90°-82°. This is consistent with our observations. For Sector I (315°/25°) regional toppling is not possible assuming a joint friction angle of 30° for interlayer slip between two adjacent blocks. For the entire Moosfluh slope with average inclination (Θ) of 29° and a normal to foliation (γ) of 10° the friction angle of the toppling layer surfaces ϕ must be less than 19° (Figure 10b). As interlayer slip is expected to occur also along cataclastic faults with gouge, or along weathered schist, friction angles smaller 30° are expected to occur at least locally. Thus, toppling along deep and steeply dipping F1 discontinuities is likely to be the dominant kinematic mode for the Moosfluh Landslide, F3 discontinuities serve as base for building of blocks in block-flexural toppling and F2 discontinuities are suitable as lateral release planes. For local rock wall inclinations of up to 75° the number of F1 discontinuities lying within the area of kinematic feasibility increases immensely from 100 counts at 39°, 150 counts at 45° to 320 counts at 75° slope dip (out of 320 measured F1 discontinuities; light red Figure 10a). Also planar/stepped planar sliding of F3 discontinuities was found to be locally possible (light blue Figure 11). Similar although not identical kinematic modes have been proposed by Kos et al. (2016).

For the surroundings of the Moosfluh Landslide, only few discontinuities lying within the range of kinematic feasibility for sliding (F3) have been measured (blue areas Figure 11b). In general F1 discontinuities show a smaller scatter and steeper dip outside the Moosfluh Landslide which is presumably related to less gravitational slope displacements. The measured F1 discontinuities are prone to toppling for slope angles between 25°-65° assuming a friction angle of 20° (red areas Figure 11b). Typical slope dips NE of Moosfluh range between 25° and 35°.

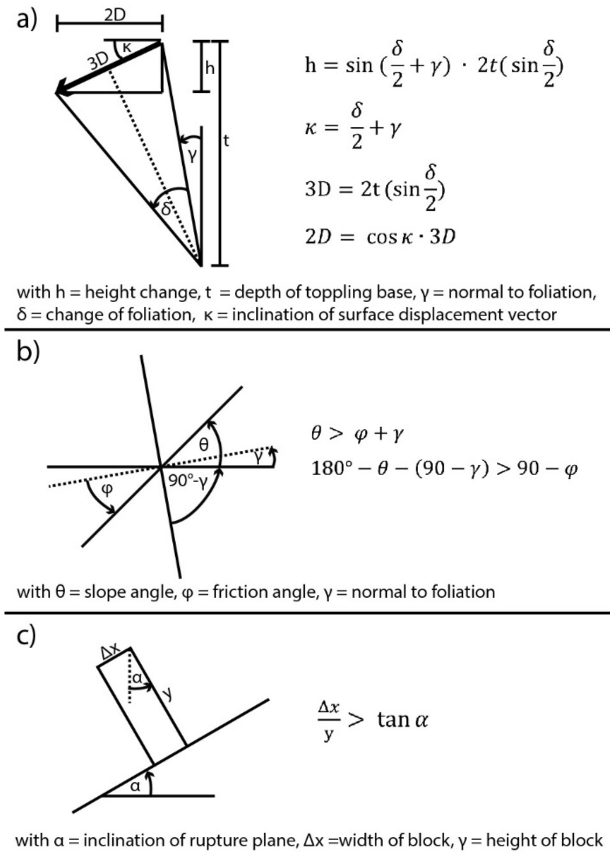

Figure 10. Geometrical constraints for toppling mechanism a) Vector displacements: Horizontal and vertical displacements on the surface depending on foliation, depth of toppling base surface and change of foliation due to toppling. b) Interlayer slip: Condition for the dip of the foliation depending on the friction angle for interlayer slip to occur (modified after Goodman and Bray, 1976). c) Block Geometry: The block geometry depends on depth and width of the block and decides if a block is stable or out of balance (modified after Goodman and Bray, 1976).

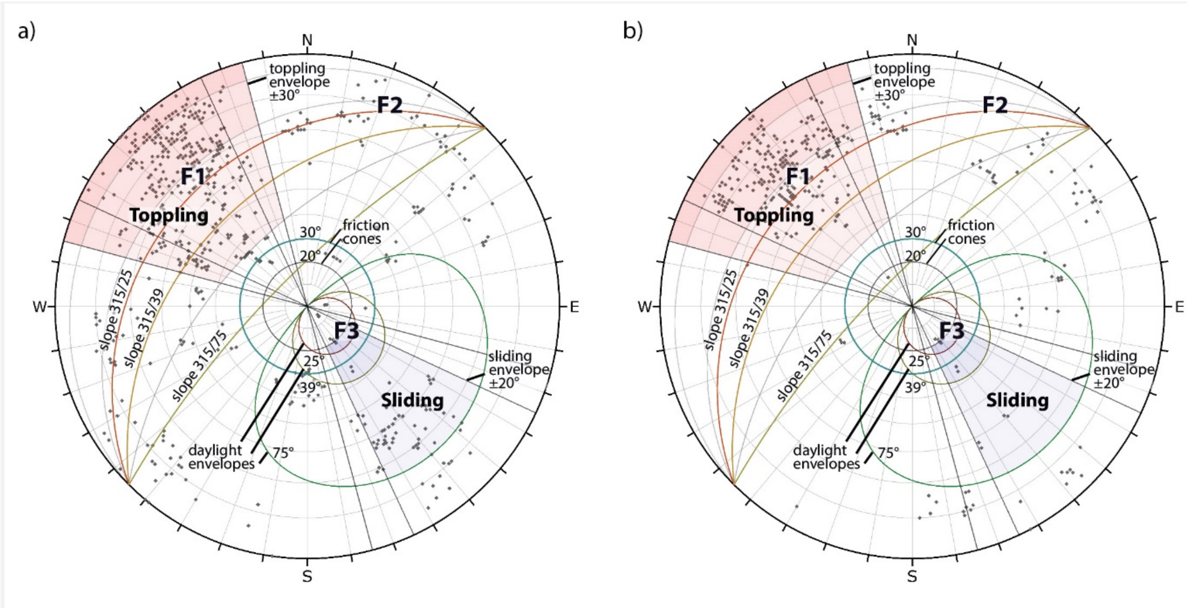

Figure 11. Kinematic analysis of structural data from the Moosfluh Landslide. a) Representing structural data from inside the Moosfluh Landslide and b) Representing structural data from outside the current instability. Shown are critical pole vector zones (slip limits) for flexural toppling in slopes steeper than 25° (dark red), 39° (solid red) and steeper than 75° (light red). Critical pole vector zones and daylight envelopes for sliding (joint set F3) are shown for slope angles less than a 25° (dark blue), 39° (solid blue) or 75° slope (light blue). All analyses are done for a friction angle of 20°; for a friction angle to 30° resulting areas prone to toppling and sliding are smaller. Slope orientations of 315/25 and 315/39 are mean orientations of slope sectors, 315/75 corresponds to a local cliff orientation. F3 planes in Figure 11b might be under-sampled.

5.2.2 Structural model of the Moosfluh Landslide as of summer 2016

Deep-seated gravitational slope deformations are landslides whose properties are mainly based on geomorphic evidences like the occurrence of morpho-structural features such as double ridges, ridge top depressions, scarps and counterscarps masked by weathering and erosion, and with present-day low rates of displacement (Agliardi et al., 2001). For the Moosfluh DSGSD toppling can be clearly identified as the dominant mode of displacement. Since the biotite gneiss occurring within the Moosfluh Landslide is expected to have a high intact strength, block or block-flexural toppling along F1 (interlayer sliding joints) and F3 cross-joints (toppling base surface) is supposed to be more important than pure flexural toppling.

The geometry and depth of the failure surface formed during deep-seated toppling (i.e. toppling hinge zone, toppling rupture plane or toppling base surface) controls the landslide volume and stability relationships. Possible failure surface geometries discussed in the literature include three different scenarios (linear, bilinear, curvilinear; Goodman and Bray, 1976; Hittinger, 1978; Pritchard and

Savigny, 1990; Goricki, 1999). To assign a subsurface geometry and investigate the paraglacial stability evolution since the LIA the maximum extents of these three geometries are explored and their probability is reviewed based on the morphological, geomechanical and geophysical constraints listed in Table 3. The three scenarios along a profile through the midst of the Moosfluh slope (Profile B Figure 3) are displayed in Figure 12 together with theoretically expected displacement vectors and the observed TPS displacements recorded in the years 2015-2016.

A planar toppling rupture plane is described by a series of columns resting on a stepped-planar base which connects the main head scarp with the valley bottom (Figure 12a; Goodman and Bray, 1976; Hittinger, 1978; Goricki, 1999). Planar toppling base surfaces result from Base Friction Table models and represent a fundamental assumption of the limit-equilibrium method proposed by Goodman and Bray (1976). Due to geometrical constraints (Figure 10c) a linear toppling base surface is characterized by a passive wedge at the top and surface deformation can be directly linked to column depth and the toppling angles.

Bilinear failure planes of flexural toppling are predicted from models with the distinct element code UDEC (Pritchard and Savigny, 1990). The bilinear failure surface daylights at the main head scarp and runs through the depth in parallel to the slope surface, until it reaches the altitude of the valley bottom from where it develops a horizontal deformation boundary (Figure 12b). The deformation field caused by bilinear flexural toppling is also characterized by a passive wedge at the subsidence zone behind the crest. For a bilinear failure plane surface displacements are expected to be generally higher than for a linear failure plane, especially at the slope toe. Based on the simulation results of Pritchard and Savigny (1990) the displacement vector plunge at the slope toe should be sub-horizontal.

Curvilinear or circular failure planes (Figure 12c) result from numerical models of flexural toppling with the distinct element code UDEC when block cohesion and tensile strength are increased and friction angles decreased with respect to the bilinear failure plane model (Pritchard 1989; Pitchard and Savigny 1990). These models further generate a greater depth of the failure surface in the central landslide section causing larger surface displacement vectors and a relatively steeply plunging displacement vector at the landslide head.

In summary the key factors leading to a differentiation of the three rupture plane geometries for toppling are rock mechanical properties (including block cohesion, tensile strength and friction angles), as well as cumulative displacement magnitudes and displacement plunge angles along profile sections. A linear rupture plane of 23° inclination results in increasing landslide depths along its profile from the Sparrhorn Cliffs to the crest (Moosfluh) of 160 m and decreasing until Tschifra (85 m) down to zero at the slopes' toe (Figure 12a). For a bilinear rupture plane depth increase from Moosfluh (190 m) up to 220 m at Alte Staffel and since the rupture plane is parallel to the surface (29°) this depth stays constant until it reaches Tschifra (200 m) where depths are decreasing again (Figure 12b). A curvilinear rupture plane results in greater depth between 300 m at Moosfluh, 340 m around Alte Staffel and 220 m at Tschifra (Figure 12c). Based on observed displacement magnitudes and vector orientations, the planar rupture surface model matches best all field observations.

The final balanced cross–sections honoring all available data through the Moosfluh Landslide up to summer 2016 (before the Moosfluh Crisis) are shown on Figure 13. The planar toppling base surface daylights at the lateral landslide margins and the landslide depth continuously decreases towards the left and right boundary. Therefore, all TPS displacements recorded since 2011 confirm the planar rupture plane model. The cumulative change in inclination of displacement vectors due to toppling depend on the in-situ position, which are in the range between 10-12.5° for 85° SE and 15-17.5° for 80° SE and match the observed toppling angles of 10° to 15° (Figure 11a). Until September 2016 no sliding is required to accommodate the long term cumulative displacements which can be derived from geomorphic evidence (Chapter 3.2) and the monitored displacements since the LIA (integration of displacement velocities shown in Figure 9). As our kinematic and structural model represents a simplification of the real geological situation, minor sliding along hinge lines of the block-flexural toppling slope is nevertheless possible.

The Moosfluh Landslide inherits a volume of around 100 Mm³ assuming a planar rupture plane, which decreases to 75 Mm³ taking into account that maximum depths are only reached at the central part and decrease towards the lateral borders (Figure 13).

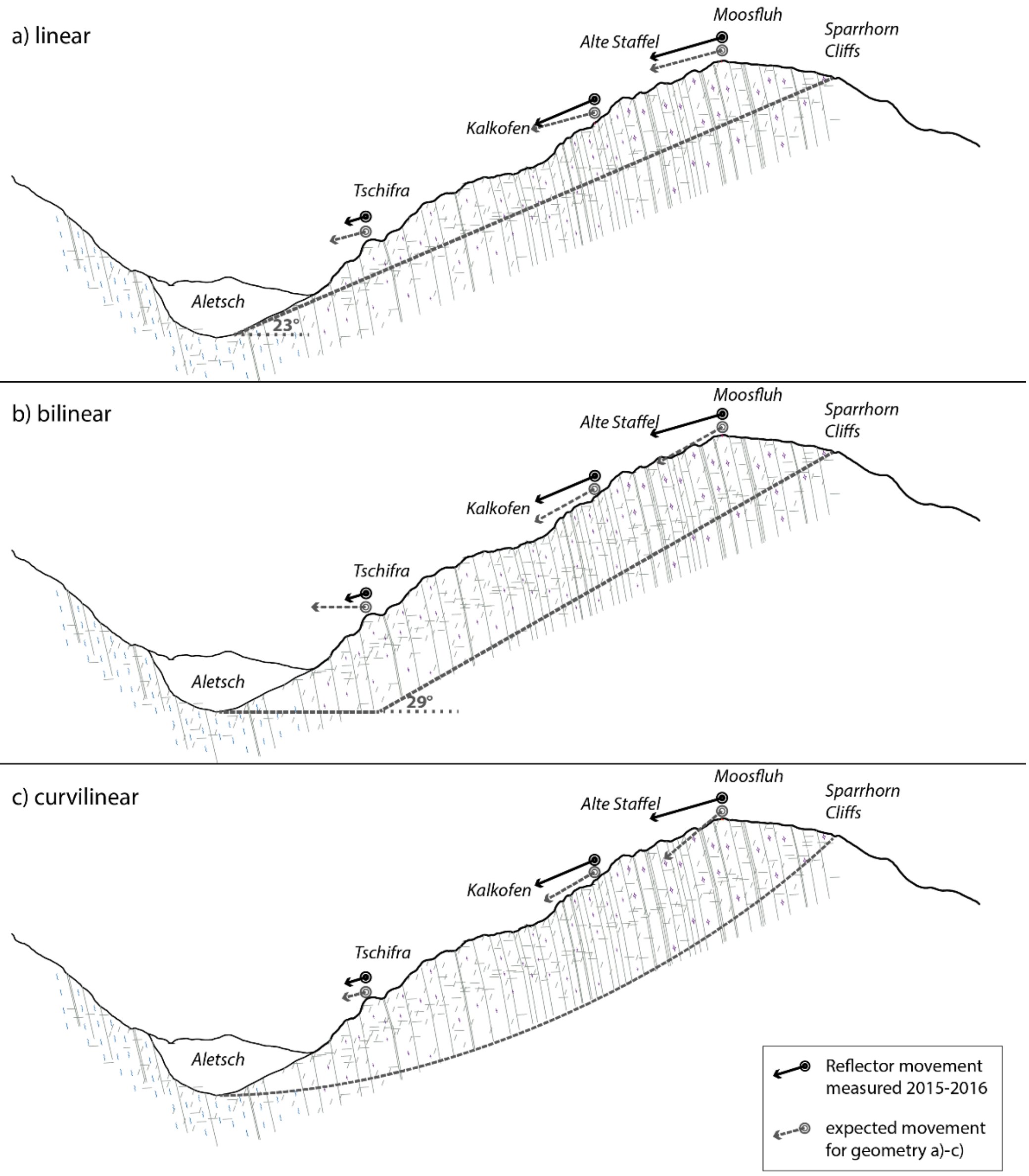

Figure 12. Possible toppling base surface geometries of the Moosfluh Landslide along Profile B (for location see Figure 3 and insert map Figure 13) with expected surface movement and measured reflector movement from 2015-2016 for (a) linear block toppling base surface with a constant base inclination of 23°, (b) bilinear toppling with flexural toppling of the lower portion of the slope and sliding of a wedge-shaped block behind the slope crest and (c) curvilinear deformation due to flexural toppling.

Table 3. Morphological, geomechanical, geophysical and historical observations at the different sectors of the Moosfluh Landslide.

Property	Sector I	Sector II	Sector III
Morphologic structures	Long (-1 km) foliation parallel asymmetric linear depressions on slope; small scarps bounding lencticular horst/graben structures;	Shorter foliation-parallel linear depressions filled with sediments; rock walls forming massive slope breaks (30 m high, 100 m long)	High slope breaks; smaller foliation-parallel up-hill facing scarps; minor foliation parallel linear depressions; oversteepened toe
Surface nature	Bedrock ridges and sediment-filled depressions, aretic moors and swamps	Bedrock ridges and sediment-filled depressions	Glacially abraded bedrock, partial till-cover
Slope dip direction/dip	315/25	315/38	315/39
Reflector movement 2014-2015: ID; 3D displacement; Azimuth; plunge; info	36; 675 mm; 310°; **-15°** No clear main scarp	35; 514 mm; 320°; **-21°**	34; 172 mm, 316°; **-14°** Rupture surface not visible at the toe
Reflector movement 2015-2016: ID; 3D displacement; Azimuth; plunge; info	36; 1450 mm; 311°; **-16°** No clear main scarp	35; 1259 mm; 318°; **-23°**	34; 438 mm, 316°; **-17°** Rupture surface not visible at the toe
Seismic investigation: ambient vibration (Kleinbrodt et al., 2017)		Shear wave velocity transition at 50 m and 100-120 m depth	
Geology	Microcline-Biotite-Gneiss	Microcline-Biotite-Gneiss and Biotite Granite	Biotite Granite
Landslide phenomena	Extended head scarp steeply dipping towards NW, extensional graben structures	Uphill-facing toppling scarps	Secondary shallow (~40 m) rockslides, e.g. at Sand
Joint sets and inclination in profile direction (ip; 322°)	F1: foliation (dip direction/dip: 137/77), high persistence (10 – 20 m), very close spacing (0.6 – 2 cm) to extremely wide spacing (> 6 m); ip: -77°w F2: (204/83), low persistence (1-3 m), wide spacing (0.6-2 m); ip: 75° F3: (320/20), medium persistence (3 – 10 m), very wide spacing (2 – 6 m); ip: 20°		
Inclination of rupture plane (α) (Goricki, 1999)	with foliation 80°-77° (γ=10°-13°) and interlayer friction angle (ϕ) of 20°-30°: **α= 20°-28°**		
Vertical displacement of moraine deposits		Egesen 10-50 m	LIA 0-10 m

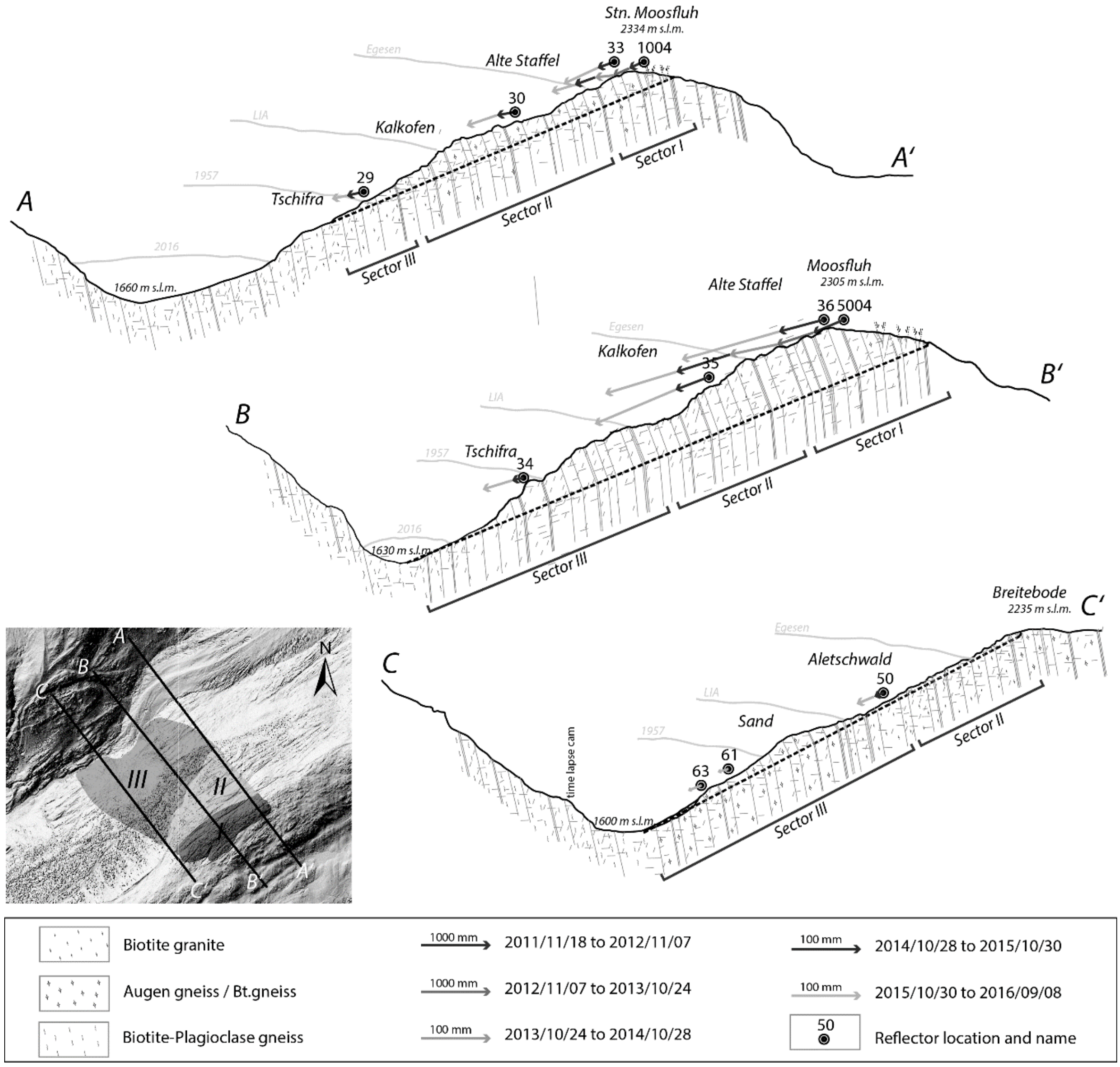

Figure 13. Geological cross sections of the Moosfluh slope based on a DEM of 2014; for location see insert map and Figure 3. Arrows are yearly displacement vectors for the time period from November 2011 until September 2016, measured by a total station and reflectors mounted on rock and labeled with numbers. Thin black lines denote the apparent orientation of foliation (average 80° into the slope) and cross joints (F2 and F3). The estimated depth of a potential rupture plane is shown by the bold black dashed line. The rupture plane shows an inclination of 23° for cross section A and B and 26° for cross section C. The glacial retreat between Egesen, LIA, 1957 and 2017 is indicated by blue lines, the locations and heights are indicated by names and numbers.

5.3 Stability evaluation in a paraglacial environment

The role of the glacial loads on slope stability has been discussed manifold, but it is unquestioned that removing the ice-cover has remarkable implications on the mechanical, thermal and hydrogeological loading conditions. Grämiger et al. (2017) show that slopes are most sensitive to ice loss in the toe region and the timing of greatest displacement coincides with first glacial unloading, leading to initiation of slope instabilities.

To better understand the role of glacial ice and changing groundwater conditions in a fully developed toppling slope we investigated the Moosfluh slope stability for different glacial conditions with a limit-equilibrium analysis assuming a stepped planar block toppling model (RockTopple from Rocscience 2017) developed after Goodman and Bray (1976). To account for the ductile nature of ice and its limited buttressing effect (McColl et al., 2010; McColl and Davis, 2013; Leith et al., 2014; Grämiger et al., 2017) glacial ice is modelled as a hydrostatic load (with ϕ_{ice}= 917 kg/m^3). Basal shear stresses due to ice flow at the glacier bed are neglected because they are limited by the yield shear stress of ice and the presence of water at the interface. These are typically in a range from 50 to 150 kPa (Paterson, 1994), an order of magnitude smaller than overburden stress during Holocene glacier cycles. We assume that the groundwater table in the fractured and permeable landslide body above the ice is generally low and controlled by a spring line mapped on the SE side of the Moosfluh ridge at an elevation of about 2100 m a.s.l. Water pressure below the ice is directly linked to the subglacial meltwater hydrology, where we assume an annually averaged water pressure corresponding to 80% of the glacier height. Therefore, the hydrostatic force of the glacial load is partly compensated by the uplifting force caused by pore water pressure.

Figure 14a shows the vertical forces acting on a single hypothetical toppling block (W_n) located near the bottom of the slope. Hydrostatic forces due to the weight of the glacier acting normal to the block surface (W_i), as well as the uplifting forces (U) and the weight of the toppling block are shown for different glacial ice loading conditions. It is obvious that for larger glacial ice loads higher resulting forces exist acting vertically downwards. Reducing ice load is usually associated with a reduced ground water level, but as long as the toppling block is completely saturated, the uplifting force corresponds to the height of the block, independently of the glacial load. The moment the slope is completely deglaciated dry conditions are assumed for the toppling block carrying now its own weight. At a certain weight of the dry block this will surpass the former force caused by glacial loading in saturated conditions.

The development of the factor of safety for a simplified Moosfluh slope geometry at Cross Section B (Figure 13), spacing of toppling joints of 15 m, friction angle of 30° for the base joints, and 19° for the toppling joints, is shown in Figure 14b together with the height of ice above the valley bottom during the same period of observation. It can be seen that the factor of safety drops non-linearly between the LIA maximum and 2007, when the height of ice above the valley bottom melted down to 100 m. Since 2007, the unsaturated conditions at the slope toe would lead to an increase in stability. However, this model assumes stable material properties and no progressive damage especially along the toppling base surface. A friction angle of only 19° degrees can be explained by field observations showing very smooth sheet silicate coated surfaces in all active toppling fractures.

This simplified toppling model can also be used to address the long term degradation of rock mass strength during the Holocene. A substantial part of this weakening might be attributed to a reduction of frictional strength along the mainly steeply dipping foliation parallel to weak schist and cataclastic fault gauge layers, as the friction angles of interlayer slip zones are the most critical factor for the observed slope kinematics. Discontinuum models of Grämiger et al. (2017) imply that the failure of intact rock bridges (in comparison to the peak LGM damage) since the LGM ranges between 4%-30%. If we would include only 4% rock bridges along toppling joints Jenning's formula (1970) would predict an equivalent cohesion of 440 kPa and friction angle of 22° leading to large factors of safety and explaining slope stability in earlier glacial cycles.

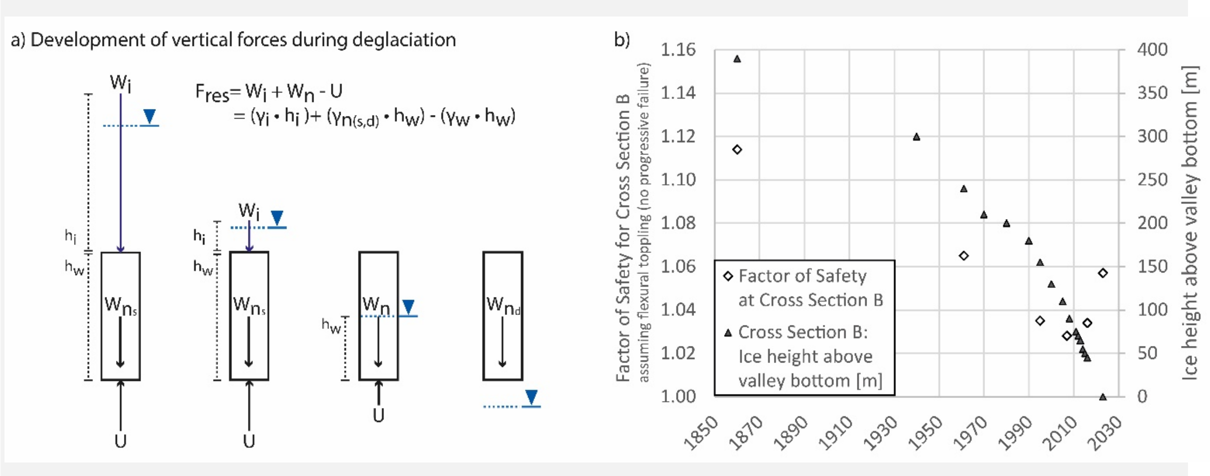

Figure 14. Slope stability and vertical forces acting on a single toppling block with ice load (W_i), weight of the block (W_n) and water pressure (U). a) Development of vertical forces acting on a toppling block during deglaciation showing high resulting forces caused by glacial ice load (W_i), block weight (W_n) and water pressure (U) for high glacial levels and lowest forces when ice level reaches bedrock surface; b) Development of the Factor of Safety for the Moosfluh toppling slope from 1850 until 2016 for changing ice loads and ground water level based on the block toppling model of Goodman and Bray (1976) with model parameters of a simplified geometry of Cross Section B, 15 m toppling joint spacing, 30° base joint friction angle, 19° toppling joint friction angle and no cohesion.

6 Discussion

This paper mainly focuses on the study of the Moosfluh DSGSD displacement history after the LIA deglaciation. Nevertheless, field data and previous work (Grämiger et al., 2017) have shown that the progressive evolution of Moosfluh may imply relationships between the DSGSD onset and older deglaciation periods (Egesen or even Last Glacial Maximum (LGM)). Also recent modeling results of Riva et al. (2018) suggest that very long time scales (thousands of years) may be required in a paraglacial context to accumulate rock mass damage leading to the onset of measurable rock slope deformations.

The regional altitude depression and historical images of a locally displaced Egesen lateral moraine at Alte Staffel clearly indicate a landslide activity after the Egesen stadial. These gravitational slope displacements seem to be roughly double in cumulative magnitude in comparison to the displacements which have been recorded by the displaced LIA moraine. Movement magnitudes as observed since the end of the last century cannot have occurred during previous deglaciations, as the cumulative displacement magnitudes of the Moosfluh Landslide are limited and have been constrained by balanced cross-sections. On the other hand glacial reconstruction by Grämiger et al. (2017) showed that the Great Aletsch Glacier has retreated beyond the area of the current Moosfluh Landslide at least five times after the Egesen stadial. Unfortunately landslide activity during Holocene glacial retreats cannot be investigated in detail as clear trimlines or deposits have been destroyed by the LIA glaciation. However, the response of the Moosfluh slope being exposed to similar boundary conditions several times during the Holocene cannot be uniform, and a strongly increased displacement rate can be documented since the LIA deglaciation. This increase in slope movements must be related to progressive degradation of rock slope strength during the Holocene glacial cycles, especially during the LIA.

Numerical discontinuum models of Grämiger et al. (2016) suggest that this rock mass damage is not a result of purely mechanical loading or unloading from glacial erosion and variations in ice overburden, but also strongly regulated by stress-changes from thermo-mechanical and hydro-mechanical "shocks" and loading cycles. Grämiger et al. (2017) suggested that major damage propagation along pre-existing discontinuities occurred during Egesen ice retreat, while minor damage events followed Holocene advance and retreat cycles. Assuming effective peak/residual friction angles along foliation planes of 35°/27° and along foliation parallel faults of 27°/27°, cumulative displacements modeled for the Moosfluh slope for a simplified late- and postglacial scenario with 500 annual thermo-hydro-mechanical cycles are in the order of 0.1-0.2 m (Grämiger et al., 2016). This simulation is assumed to represent the damage in the stable Moosfluh slope during the preparatory phase before the onset of landslide activity.

Simulating the complete transition from a stable slope into a fully developed and differentiated landslide (the entire life cycle) was recently carried out by Riva et al. (2018) with a damage based continuum model combined with a time-to-failure law and a simplified description of water occurrence in the slope during its damage evolution. The non-linear decay of deformation modulus at the finite element scale allowed them to evaluate the spatial pattern and track the temporal evolution of brittle damage on the slope scale. However, thermo-mechanical effects and complexities of the glacier retreat and re-advance history were not accounted for. This model was applied and calibrated to a compound suspended rockslide in Spriana Valley and model results suggest that complete rockslide differentiation was only reached during middle Holocene only. During the next 6 ka until present day, progressive slope failure continued, with the upslope retrogression of the basal shear zone to a prehistoric headscarp. According to Riva et al. (2018) this evolution is associated with further nonlinear increase of displacement rates up to 20 mm/a , consistent with present-day measured values, and vertical displacement at the rockslide headscarp reaching 80 m.

Our observations support this suggested very long term duration of paraglacial rock slope adjustment, the onset of large slope instability in discrete evolutionary stages, and the complex spatial evolution of slope deformations in response to deglaciation. The data presented in this paper suggest that landslide activity leading to cumulative displacements in the order of several tens of meters since the Egesen stadial, presumably started during the Holocene. After several glacial advances/retreats during the Holocene, and many thousands of annual thermo-hydro-mechanical loading cycles, the Moosfluh instability has reached a critical state of stability, most probably only during the last decades. We can therefore allocate subglacial rock mass damage or weakening also to the LIA glaciation. Aerial Digital Photogrammetry from before the mid '90s indicates limited landslide displacements (>0.01m/a). Since this time the slope has accelerated from 0.05-0.1 m/a until 2011 to more than 0.2 m/a in 2007 and >1 m/a in 2016 (based on DIC, D-InSAR displacements and TPS measurements).

DIC data also gives an idea of the spatial displacement pattern of the instability, showing the main area of movement shifted up-valley with ongoing glacial retreat, changing from a local displacement at the ridge area (2005-2008) to a comprehensive displacement along the whole slope in recent years (2008-2016). DIC analysis allows for confining a clear limitation of the unstable area. Similar to some other case studies our analyses show a temporal relationship between glacial retreat and landslide activity (Evans and Clague, 1994; Holm et al., 2004; Oppikofer et al., 2008; Strozzi et al., 2010; Clayton et al., 2013; McColl and Davies, 2013; Kos et al. 2016). Figure 9a shows that the Moosfluh slope started to accelerate from 1995 to 2007, at a time when the glacier tongue was still more than 400 m further downslope. However, at this time, the glacier dramatically changed its rate of yearly height loss from -2 m/a to -6 m/a having an average ice height of 170 m at the slope toe in 1995

(Figure 9b). In 2007, when the glacier reached the northwestern lateral border of the instability, displacement rates of the Moosfluh slope increased from cm/a to several dm/a and reached 1.5 m/a until September 2016 (before the crisis started). At this time, the left lateral landslide boundary has been ice-free for almost 10 years and the glacier tongue lost 350 m of length since 2007.

7 Summary

This study is a continuation of previous investigations of the Moosfluh deep-seated gravitational slope deformation (DSGSD) in a paraglacial context, as described by Strozzi et al. (2010), Kos et al. (2016) and Grämiger (2017). In this contribution we focus on the detailed structure, kinematics and displacement evolution of the Moosfluh landslide using new historical aerial imagery, Aerial Digital Photogrammetry (ADP), Digital Image Correlation (DIC) and total station displacement monitoring (TPS). We have explored the morphological phenomena of the paraglacial Moosfluh DSGSD and related its landslide movement indicators, such as displaced Egesen and LIA moraine walls, to the Lateglacial and Holocene deglaciation history of the Great Aletsch Glacier. Based on geometrical and mechanical constraints as well as displacement vector analyses the subsurface structures of the Moosfluh Landslide have been systematically investigated and for the first time balanced cross-sections through the toppling landslide could be derived. Finally we have explored the evolution of the landslide damage and rock strength degradation in a paraglacial context and show with limit-equilibrium-analyses how stress changes associated with unloading glacial ice and changing groundwater levels generate critical rock slope stability conditions in the last few decades.

Using historical aerial imagery and photogrammetric analysis techniques allows a quantification of historic displacements showing small displacement rates of <1 cm/a since LIA ice retreat (1860) until 1997, an increased rock slope activity from 1997-2007 (up to 10 cm/a) and a massive acceleration until fall 2016 to >1m/a. Digital Image Correlation (DIC) of ortho-images obtained from national ortho-image mosaics could further be used to derive 2D-displacement fields and were especially helpful in constraining landslide boundaries. The installation of two robotic total stations in 2013 and 2014 led to the acquisition of continuous 3D displacement data at 80 reflector positions. TPS measurements allowed for conclusive kinematic and structural interpretations of the Moosfluh instability.

We show that until September 2016 toppling along deep and steeply dipping foliation parallel (F1) discontinuities is the dominant kinematic mode, slope parallel (F3) discontinuities serve as base for building of block-flexural toppling blocks, and F2 discontinuities serve as lateral release planes. The Moosfluh landslide has a planar toppling base surface connecting the valley bottom with a head scarp located behind the Moosfluh ridge. The landslide velocity distributions are related to an uneven topography above this planar base, and relatively uniform toppling block rotations in the range of 10° to 15° This geometry of the toppling base leads to a deep-seated gravitational slope instability with a volume of ~75 Mm^3, a depth of up to 170 m and a 23°-27° dipping toppling base surface.

Reconstructing the long-term evolution of the Moosfluh DSGSD showed that paraglacial rock slope adjustment in a paraglacial context can undergo thousands of years and is composed of discrete evolutionary stages. Displacements between the Egesen (~12ky BP) and the LIA (1850) are in the same magnitude as between the LIA (1850) and 2016, indicating a strongly increased displacement rate since the LIA deglaciation. This can be related to progressive degradation of rock slope strength during multiple Holocene glacial cycles and especially the LIA. During this recent stage of the Moosfluh slope evolution we see temporal correlations between changes in the Moosfluh rock slope stability, velocity and glacial ice downwasting at the landslide toe. The landslide activity increased considerably from 2007 on, a time period when the height of ice above the valley bottom melted down to 100 m. At the same time the stability of the landslide reached its minimal level, as derived from a limit-equilibrium analysis with the stepped planar block toppling model of Goodman and Bray (1976), considering variable ice load and water pressures since the LIA. As such our investigations document in great detail how a large slope instability evolves geomorphologically and structurally in a paraglacial context.

8 Acknowledgements

We thank Peter Schwitter (Natural Hazard Observation Service Naters) for multiple supports in the field, Laudo Albrecht (ProNatura Center Aletsch) and the Community of Riederalp (Peter Albrecht) for enabling the construction of a monitoring network within the protected areas of the Aletsch Forest, Andreas Wieser for providing advice on TPS monitoring, Lorenz Grämiger for supporting the first total station setup and Reto Seifert for designing and constructing two total stations in this high alpine environment. Additional biannual geodetic surveying of the Riederalp-Blausee-Moosfluh monitoring network was conducted by PLANAX AG Visp and directed by Michael Ruppen (Odilo Schmid & Partner AG, Brig, Switzerland). Thanks to Jordan Aaron for fruitful discussions, Susan Ivy-Ochs for input on the behavior of moraine deposits and former BSc student J. Schmid for her contributions in historical aerial photogrammetry. Special thanks to Stefan Conzett for his field assistance and advice on geodetic monitoring. We finally acknowledge and greatly appreciated the careful and constructive reviews of Sam McColl, two anonymous reviewers and the editor Markus Stoffel. This project was funded by the Swiss National Science Foundation (projects 146593 and 172492).

9 References

Abele, G., 1974. Bergstürze in den Alpen : ihre Verbreitung, Morphologie u. Folgeerscheinungen. Deutscher Alpenverein: Wissenschaftliche Alpenvereinshefte ; H. 25: 230.

Adam Technology Inc., 2012. 3DM CalibCam and 3DM Analyst. Software and user manuals, Version 2.5.0 (http:\\www.adamtech.com.au).

Agliardi, F., Crosta, G. and Zanchi, A., 2001. Structural constraints on deep-seated slope deformation kinematics. Engineering Geology, 59(1-2): 83-102.

Alley, R.B., Meese, D.A., Shuman, C.A., Gow, A.J., Taylor, K.C., Grootes, P.M., White, J.W.C., Ram, M., Waddington, E.D., Mayewski, P.A. and Zielinski, G.A., 1993. Abrupt increase in Greenland snow accumulation at the end of the Younger Dryas. Nature, 362(6420): 527-529.

Ambrosi, C. and Crosta, G.B., 2006. Large sackung along major tectonic features in the Central Italian Alps. Engineering Geology, 83(1-3): 183-200.

Arguile, R., Beaumont, T.,Blackford, S.,Brink, A.,Brown, G.,Burland, J.,Calvert, J.,Crofts, R.,Gordon, D.,Grifiths, F.,Hinch, L.,Holt, J.,Jordan, P.,Lawrence, C.,McDermott, A.,Rawlings, G.,Ritchie, W.,Roberts, D.,Spencer, F.,Stroud, M.,Webster, R.,Wright, E., 1982. LAND SURFACE EVALUATION FOR ENGINEERING PRACTICE. Quarterly Journal of Engineering Geology, 15(4): 265-316.

Ballantyne, C., 2002. Paraglacial geomorphology. Quaternary Science Reviews, 21: 83.

Ballantyne, C.K. and Stone, J.O., 2013. Timing and periodicity of paraglacial rock-slope failures in the Scottish Highlands. Geomorphology, 186: 150-161.

Ballantyne, C.K., Wilson, P., Gheorghiu, D. and Rodes, A., 2014. Enhanced rock-slope failure following ice-sheet deglaciation: timing and causes. Earth Surface Processes and Landforms, 39(7): 900-913.

Bigot-Cormier, F., Braucher, R., Bourles, D., Guglielmi, Y., Dubar, M. and Stephan, J.F., 2005. Chronological constraints on processes leading to large active landslides. Earth and Planetary Science Letters, 235(1-2): 141-150.

Clayton, A., Stead, D., Kinakin, D. and Wolter, A., 2017. Engineering geomorphological interpretation of the Mitchell Creek Landslide, British Columbia, Canada. Landslides: 1-21.

Coquin, J., Mercier, D., Bourgeois, O., Cossart, E. and Decaulne, A., 2015. Gravitational spreading of mountain ridges coeval with Late Weichselian deglaciation: impact on glacial landscapes in Trollaskagi, northern Iceland. Quaternary Science Reviews, 107: 197-213.

Corominas, J. and Moya, J., 2008. A review of assessing landslide frequency for hazard zoning purposes. Engineering Geology, 102(3): 193-213.

Cossart, E., Barucher, R., Fort, M., Bourles, D. and Carcaillet, J., 2008. Slope instability in relation to glacial debuttressing in alpine areas (Upper Durance catchment, southeastern France): Evidence from field data and 10Be cosmic ray exposure ages. Geomorphology, 95: 24.

Cruden, D.M. and Hu, X.Q., 1993. Exhaustion and steady state models for predicting landslide hazards in the Canadian Rocky Mountains. Geomorphology, 8(4): 279-285.

Dahl-Jensen, D., Albert, M.R., Aldahan, A., Azuma, N., Balslev-Clausen, D., Baumgartner, M., Berggren, A.M., Bigler, M., Binder, T., Blunier, T., Bourgeois, J.C., Brook, E.J., Buchardt, S.L., Buizert, C., Capron, E., Chappellaz, J., Chung, J., Clausen, H.B., Cvijanovic, I., Davies, S.M., Ditlevsen, P., Eicher, O., Fischer, H., Fisher, D.A., Fleet, L.G., Gfeller, G., Gkinis, V., Gogineni, S., Goto-Azuma, K., Grinsted, A., Gudlaugsdottir, H., Guillevic, M., Hansen, S.B., Hansson, M., Hirabayashi, M., Hong, S., Hur, S.D., Huybrechts, P., Hvidberg, C.S., Iizuka, Y., Jenk, T., Johnsen, S.J., Jones, T.R., Jouzel, J., Karlsson, N.B., Kawamura, K., Keegan, K., Kettner, E., Kipfstuhl, S., Kjaer, H.A., Koutnik, M., Kuramoto, T., Koehler, P., Laepple, T., Landais, A., Langen, P.L., Larsen, L.B., Leuenberger, D., Leuenberger, M., Leuschen, C., Li, J., Lipenkov, V., Martinerie, P., Maselli, O.J., Masson-Delmotte, V., McConnell, J.R., Miller, H., Mini, O., Miyamoto, A., Montagnat-Rentier, M., Mulvaney, R., Muscheler, R., Orsi, A.J., Paden, J., Panton, C., Pattyn, F., Petit, J.R., Pol, K., Popp, T., Possnert, G., Prie, F., Prokopiou, M., Quiquet, A., Rasmussen, S.O., Raynaud, D., Ren, J., Reutenauer, C., Ritz, C., Rockmann, T., Rosen, J.L., Rubino, M., Rybak, O., Samyn, D., Sapart, C.J., Schilt, A., Schmidt, A.M.Z., Schwander, J., Schuepbach, S., Seierstad, I., Severinghaus, J.P., Sheldon, S., Simonsen, S.B., Sjolte, J., Solgaard, A.M., Sowers, T., Sperlich, P., Steen-Larsen, H.C., Steffen, K., Steffensen, J.P., Steinhage, D., Stocker, T.F., Stowasser, C., Sturevik, A.S., Sturges, W.T., Sveinbjornsdottir, A., Svensson, A., Tison, J.L., Uetake, J., Vallelonga, P., van de Wal, R.S.W., van der Wel, G., Vaughn, B.H., Vinther, B., Waddington, E., Wegner, A., Weikusat, I., White, J.W.C., Wilhelms, F., Winstrup, M., Witrant, E., Wolff, E.W., Xiao, C., Zheng, J. and Community, N., 2013. Eemian interglacial reconstructed from a Greenland folded ice core. Nature, 493(7433): 489-494.

Darnault, R., Rolland, Y., Braucher, R., Bourles, D., Revel, M., Sanchez, G. and Bouissou, S., 2012. Timing of the last deglaciation revealed by receding glaciers at the Alpine-scale: impact on mountain geomorphology. Quaternary Science Reviews, 31: 127-142.

Delacourt, C., Allemand, P., Berthier, E., Raucoules, D., Casson, B., Grandjean, P., Pambrun, C. and Varel, E., 2007. Remote-sensing techniques for analysing landslide kinematics: a review. Bulletin De La Societe Geologique De France, 178(2): 89-100.

Dortch, J.M., Owen, L.A., Haneberg, W.C., Caffee, M.W., Dietsch, C. and Kamp, U., 2009. Nature and timing of large landslides in the Himalaya and Transhimalaya of northern India. Quaternary Science Reviews, 28(11-12): 1037-1054.

Evans, S.G. and Clague, J.J., 1994. RECENT CLIMATIC-CHANGE AND CATASTROPHIC GEOMORPHIC PROCESSES IN MOUNTAIN ENVIRONMENTS. Geomorphology, 10(1-4): 107-128.

Fey, C., Wichmann, V. and Zangerl, C., 2017. Reconstructing the evolution of a deep seated rockslide (Marzell) and its response to glacial retreat based on historic and remote sensing data. Geomorphology, 298: 72-85.

Furrer, H., 1948. Das Sackungsgebiet von Greich-Goppisberg, nördlich Mörel, und der Riederhornstollen (Oberwallis). Eclogae Geologicae Helvetiae, 41/42: 6.

Glabsch, J., Heunecke, O., Schuhbäck, S., 2009. Monitoring the Hornbergl landslide using a recently developed low cost GNSS sensor network. Journal of Applied Geodesy, 3(3): 14.

Glaciological Reports, -. 1881-2017. "The Swiss Glaciers" Yearbooks of the Cryospheric Commission of the Swiss Academy of Sciences (SCNAT) published since 1964 by the Labratory of Hydraulics, Hydrology and Glaciology (VAW) of ETH Zürich, No. 1-126((http://glaciology.ethz.ch/swiss-glaciers/)).

Glueer, F., 2019. Monitoring and analysis of interactions between the retreating Aletsch glacier and adjacent rock slope instabilities, ETH Zurich, 124 pp.

Goodman, R., Bray, J., 1976. Toppling of Rock Slopes. Proc. Specialty Conference on Rock Engineering for Foundations and Slopes. Boulder, Colorado, ASCE, 2: 34.

Goodman, R.E., 1989. Introduction to Rock Mechanics. John Wiley & Sons.

Goricki, A., 1999. Base Friction Versuche für felsmechanische Kluftkörpermodelle. Diplomarbeit TU Graz, Institut für Felsmechanik und Tunnelbau: 86.

Grämiger, L., 2017. Beyond debuttressing: Thermo-hydro-mechanical rock slope damage during glacial cycles, ETH Zurich, 135 pp.

Gramiger, L.M., Moore, J.R., Gischig, V.S., Ivy-Ochs, S. and Loew, S., 2017. Beyond debuttressing: Mechanics of paraglacial rock slope damage during repeat glacial cycles. Journal of Geophysical Research-Earth Surface, 122(4): 1004-1036.

Grämiger, L.M., Moore, J.R., Gischig, V.S., Ivy-Ochs, S. and Loew, S., 2017. Beyond debuttressing: Mechanics of paraglacial rock slope damage during repeat glacial cycles. Journal of Geophysical Research: Earth Surface, 122(4): 1004-1036.

Gramiger, L.M., Moore, J.R., Gischig, V.S. and Loew, S., 2018. Thermomechanical Stresses Drive Damage of Alpine Valley Rock Walls During Repeat Glacial Cycles. Journal of Geophysical Research-Earth Surface, 123(10): 2620-2646.

Gunzburger, Y., Merrien-Soukatchoff, V. and Guglielmi, Y., 2005. Influence of daily surface temperature fluctuations on rock slope stability: case study of the Rochers de Valabres slope (France). International Journal of Rock Mechanics and Mining Sciences, 42(3): 331-349.

Haeuselmann, P., Granger, D.E., Jeannin, P.-Y. and Lauritzen, S.-E., 2007. Abrupt glacial valley incision at 0.8 Ma dated from cave deposits in Switzerland. Geology, 35(2): 143-146.

Heim, A., 1932. Bergsturz und Menschenleben. Zürich : Fretz & Wasmuth: 218.

Hippolyte, J.-C., Bourles, D., Leanni, L., Braucher, R., Chauvet, F. and Lebatard, A.E., 2012. Be-10 ages reveal > 12 ka of gravitational movement in a major sackung of the Western Alps (France). Geomorphology, 171: 139-153.

Hittinger, M., 1978. Numerical analysis of toppling failures in jointed rock.

Hocking, G., 1974. A method for distinguishing between single and double plane sliding of tetrahedal wedges. International Journal of Rock Mechanics and Mining Sciences & Geomechanics Abstracts, 13: 2.

Holm, K., Bovis, M. and Jakob, M., 2004. The landslide response of alpine basins to post-Little Ice Age glacial thinning and retreat in southwestern British Columbia. Geomorphology, 57(3-4): 16.

Holzhauser, H., 1995. Gletscherschwankungen innerhalb der letzten 3200 Jahre am Beispiel des Grossen Aletsch- und des Gornergletschers. Neue Ergebnisse. vdf Hochschulverlag AG an der ETH Zürich: 22.

Holzhauser, H., Magny, M. and Zumbühl, H., 2005. Glacier and lake-level variations in west-central Europe over the last 3500 years. The Holocene, 15(6): 13.

Huggel, C., Clague, J.J. and Korup, O., 2012. Is climate change responsible for changing landslide activity in high mountains? Earth Surface Processes and Landforms, 37(1): 77-91.

Huttenlocher, H., 1933. Ergänzende Bemerkungen zur Geologie und Petrographie des südwestlichen Aarmassivs. Schweizerische mineralogische und petrographische Mitteilungen, 13(1): 13.

Ivy-Ochs, S., 2015. GLACIER VARIATIONS IN THE EUROPEAN ALPS AT THE END OF THE LAST GLACIATION. Cuadernos De Investigacion Geografica, 41(2): 295-315.

Ivy-Ochs, S., Kerschner, H., Reuther, A., Preusser, F., Heine, K., Maisch, M., Kubik, P.W. and Schlüchter, C., 2008. Chronology of the last glacial cycle in the European Alps. Journal of Quaternary Science, 23(6-7): 559-573.

Ivy-Ochs, S. and Kober, F., 2008. Surface exposure dating with cosmogenic nuclides. Eiszeitalter Und Gegenwart : Jahrbuch Der Deutschen Quartärvereinigung, 57(1/2): 31.

Ivy-Ochs, S., Poschinger, A.v., Synal, H.A. and Maisch, M., 2009. Surface exposure dating of the Flims landslide, Graubünden, Switzerland. Geomorphology, 103(1): 104-112.

Jennings, J.E., 1970. A mathematical theory for the calculation of the stability of open cast mines. Planning open pit mines: Proceedings of the Symposium on the Theoretical Background to the Planning of Open Pit Mines with Special Reference to Slope Stability(Johannesburg, Republic of South Africa: Balkema (A.A.)): 16.

Joerin, U.E., Stocker, T.F. and Schluchter, C., 2006. Multicentury glacier fluctuations in the Swiss Alps during the Holocene. Holocene, 16(5): 697-704.

Jouvet, G., Huss, M., Funk, M. and Blatter, H., 2011. Modelling the retreat of Grosser Aletschgletscher, Switzerland, in a changing climate. Journal of Glaciology, 57(206): 1033-1045.

Kelly, M., Kubik, P., Von Blanckenburg, F. and Schluechter, C., 2004. Surface exposure dating of the Great Aletsch Glacier Egesen moraine system, western Swiss Alps, using the cosmogenic nuclide10Be. Journal of Quaternary Science, 19(5): 431-441.

Kos, A., Amann, F., Strozzi, T., Delaloye, R., von Ruette, J. and Springman, S., 2016. Contemporary glacier retreat triggers a rapid landslide response, Great Aletsch Glacier, Switzerland. Geophysical Research Letters, 43(24): 12466-12474.

Labhart, T., 1965. Petrotektonische Untersuchungen am Südrand des Aarmassivs, nördlich Naters (Wallis, Schweiz). Beiträge zur geologischen Karte der Schweiz, 154(Diss. Univ. Bern): 81.

Lambiel, C. and Delaloye, R., 2004. Contribution of real-time kinematic GPS in the study of creeping mountain permafrost: Examples from the Western Swiss Alps. Permafrost and Periglacial Processes, 15(3): 229-241.

Lang, A., Moya, J., Corominas, J., Schrott, L. and Dikau, R., 1999. Classic and new dating methods for assessing the temporal occurrence of mass movements. Geomorphology, 30(1): 33-52.

Leith, K., Moore, J.R., Amann, F. and Loew, S., 2014. Subglacial extensional fracture development and implications for Alpine Valley evolution. Journal of Geophysical Research-Earth Surface, 119(1): 62-81.

Loew, S., Gischig, V., Glueer, F., Seifert, R., and Moore, J., 2017. Multidisciplinary monitoring of progressive failure processes in brittle rock slopes. Rock mechanics and engineering, 4(20): 34.

Maisch, M., Wipf, B., Denneler, B., Battaglia, J. and Benz, C., 1999. Die Gletscher der Schweizer Alpen : Gletscherhochstand 1850, aktuelle Vergletscherung, Gletscherschwund-Szenarien. Schlussbericht NFP 31, vdf Hochschulverlag: 373.

Manconi, A., Kourkouli, P., Caduff, R., Strozzi, T. and Loew, S., 2018. Monitoring Surface Deformation over a Failing Rock Slope with the ESA Sentinels: Insights from Moosfluh Instability, Swiss Alps. Remote Sensing, 10(5): 672.

Markland, J.T., 1972. A useful technique for estimating the stability of rock slopes when rigid wedge sliding type of failure is expected. Imperial College Rock Mechanics Research Report, 19: 10.

Massonnet, D. and Feigl, K.L., 1998. Radar interferometry and its application to changes in the earth's surface. Reviews of Geophysics, 36(4): 441-500.

McColl, S., 2012. Paraglacial rock-slope stability. Geomorphology 153–154 16.

McColl, S., Davies, T., McSaveney, M., 2010. Glacier retreat and rock-slope stability: debunking debuttressing. 11th Congress of the International Association for Engineering Geology and the Environment, edited by G. Active, Auckland, New Zealand: 8.

McColl, S.T. and Davies, T.R.H., 2013. Large ice-contact slope movements: glacial buttressing, deformation and erosion. Earth Surface Processes and Landforms, 38(10): 1102-1115.

Mercier, D., Coquin, J., Feuillet, T., Decaulne, A., Cossart, E., Jonsson, H.P. and Smundsson, D., 2017. Are Icelandic rock-slope failures paraglacial? Age evaluation of seventeen rock-slope failures in the Skagafjorour area, based on geomorphological stacking, radiocarbon dating and tephrochronology. Geomorphology, 296: 45-58.

Muttoni, G., Carcano, C., Garzanti, E., Ghielmi, M., Piccin, A., Pini, R., Rogledi, S. and Sciunnach, D., 2003. Onset of major Pleistocene glaciations in the Alps. Geology, 31(11): 989-992.

Nicolussi, K. and Schluchter, C., 2012. The 8.2 ka event-Calendar-dated glacier response in the Alps. Geology, 40(9): 819-822.

Oppikofer, T., Jaboyedoff, M. and Keusen, H.-R., 2008. Collapse at the eastern Eiger flank in the Swiss Alps. Nature Geoscience, 1: 531.

Oppikofer, T., Saintot, A., Hermanns, R.L., Böhme, M., Scheiber, T., Gosse, J. and Dreiås, G.M., 2017. From incipient slope instability through slope deformation to catastrophic failure — Different stages of failure development on the Ivasnasen and Vollan rock slopes (western Norway). Geomorphology, 289: 96-116.

Paterson, W.S.B., 1994. 5 - Structure and Deformation of Ice, The Physics of Glaciers (Third Edition). Pergamon, Amsterdam, pp. 78-102.

PLANAX AG, 2011-2016. 6/8 CGD-B Riederalp-Blausee-Moosfluh Überwachung. Ingenieure, Geometer, Raumplaner, dipl. Ingenieure ETH/SIA/USIC, pat. Ing.-Geometer, Napoleonstrasse 17, 3930 Visp.

Prager, C., Zangerl, C., Patzelt, G. and Brandner, R., 2008. Age distribution of fossil landslides in the Tyrol (Austria) and its surrounding areas. Natural Hazards and Earth System Sciences, 8(2): 377-407.

Pritchard, M.A., 1989. Numerical modelling of large scale toppling. Thesis at the Department of Geological Sciences, The University of British Columbia: 193.

Pritchard, M.A. and Savigny, K.W., 1990. NUMERICAL MODELING OF TOPPLING. Canadian Geotechnical Journal, 27(6): 823-834.

Riva, F., Agliardi, F., Amitrano, D. and Crosta, G.B., 2018. Damage-Based Time-Dependent Modeling of Paraglacial to Postglacial Progressive Failure of Large Rock Slopes. Journal of Geophysical Research-Earth Surface, 123(1): 124-141.

Scambos, T.A., Dutkiewicz, M.J., Wilson, J.C. and Bindschadler, R.A., 1992. APPLICATION OF IMAGE CROSS-CORRELATION TO THE MEASUREMENT OF GLACIER VELOCITY USING SATELLITE IMAGE DATA. Remote Sensing of Environment, 42(3): 177-186.

Schimmelpfennig, I., Schaefer, J.M., Akcar, N., Ivy-Ochs, S., Finkel, R.C. and Schluchter, C., 2012. Holocene glacier culminations in the Western Alps and their hemispheric relevance. Geology, 40(10): 891-894.

Schindelwig, I., Akcar, N., Kubik, P.W. and Schluchter, C., 2012. Lateglacial and early Holocene dynamics of adjacent valley glaciers in the Western Swiss Alps. Journal of Quaternary Science, 27(1): 114-124.

Seijmonsbergen, A.C., Woning, M.P., Verhoef, P.N.W. and de Graaff, L.W.S., 2005. The failure mechanism of a Late Glacial Sturzstrom in the Subalpine Molasse (Leckner Valley, Vorarlberg, Austria). Geomorphology, 66(1): 277-286.

Stead, D.E., E., 2013. Understanding the Mechanics of large Landslides. Italian Journal of Engineering Geology and Environment, Book Series((6)): 28.

Steck, A., 1968a. Die alpidischen Strukturen in den Zentralen Aaregraniten des westlichen Aarmassivs. Eclogae Geologicae Helvetiae, 61/1(4): 30.

Steck, A., 1968b. Junge Bruchsysteme in den Zentralalpen. Eclogae Geologicae Helvetiae, 61(2): 8.

Steck, A., 2011. 1269 Aletschgletscher mit Teil von 1249 Finsteraarhorn. Geolog. Atlas der Schweiz 1:25000.

Steck, A. and Hunziker, J., 1994. THE TERTIARY STRUCTURAL AND THERMAL EVOLUTION OF THE CENTRAL ALPS - COMPRESSIONAL AND EXTENSIONAL STRUCTURES IN AN OROGENIC BELT. Tectonophysics, 238(1-4): 229-254.

Stoffel, M., Tiranti, D. and Huggel, C., 2014. Climate change impacts on mass movements - Case studies from the European Alps. Science of the Total Environment, 493: 1255-1266.

Strozzi, T., Delaloye, R., Kääb, A., Ambrosi, C., Perruchoud, E. and Wegmüller, U., 2010. Combined observations of rock mass movements using satellite SAR interferometry, differential GPS, airborne digital photogrammetry, and airborne photography interpretation. Journal of Geophysical Research, 115(F1).

Strozzi, T., Kääb, A., Frauenfelder, R., Wegmueller, U., 2003. Detection and Monitoring of Unstable High-Mountain Slopes with L-Band SAR Interferometry. International Geoscience and remote Sensing Symposium 2003: 3.

Tarchi, D., Casagli, N., Moretti, S., Leva, D. and Sieber, A.J., 2003. Monitoring landslide displacements by using ground-based synthetic aperture radar interferometry: Application to the Ruinon landslide in the Italian Alps. Journal of Geophysical Research-Solid Earth, 108(B8).

Wieczorek, G. and Jaeger, S., 1996. Triggering mechanisms and depostitional rates of postglacial slopemovement processes in the Yosemite Valley, California; Geomorphologie, 15: 15.

Wyllie, D., Mah, C., 2004. Rock slope engineering Civil and Mining. Hoek, E. and Bray, J.W., Eds., Rock slope Engineering, Taylor & Francis Group, London and New York, 431 p. .

Ziegler, M., Loew, S. and Bahat, D., 2014. Growth of exfoliation joints and near-surface stress orientations inferred from fractographic markings observed in the upper Aar valley (Swiss Alps). Tectonophysics, 626: 20.

Supplementary Materials:

A Details of Moosfluh geomorphic features

Sector I: The undulating plain at the top of landslide near Moosfluh and Breitebode has about 200-300 m width and ends towards the SE at the Sparrhorn cliffs, a scarp facing facing NW (Figure 4f). These cliffs, ranging from 1 to 30 m in height, represent the SE limit of the main landslide body behind the ridge of Moosfluh. The cliffs dip between 60° and 85° to the NW and have a length of about 400 m parallel to the slope. The plane of Moosfluh inhibits several aretic depressions resulting in small moors and swamps and is interpreted as a wide extensional horst and graben structure with slope parallel uphill- and downhill-facing faults (Figure 5e) limited by the large uphill-facing scarp of the Sparrhorn cliffs. The plane is bordered in the north by a convex slope break of a 25° slope with 100 m difference in altitude before reaching the plain of Alte Staffel. This sector is characterized by several slope parallel, NE-SW trending paired depressions/ridges of up to 1 km in length (Figure 5). This generates a saw-tooth-structure with several m high uphill-facing surfaces dipping at an average of 70° into the slope, with an average spacing of 35 m. These mostly sediment filled depressions could have their origin due to glacial erosion and/or weathering of strongly sheared and incompetent mica schists within the bedrock as discussed above. Their occurrence in steep slopes of below Moosfluh suggests that they have possibly been overprinted by gravitational slope movements such as toppling (see also Section 4).

Sector II: At the plane of Alte Staffel a convex slope break introduces a 38° dipping slope terminating after 200 m of change in altitude with a concave slope break to the plain of Kalkofen. At the plane of Alte Staffel the Egesen Lateral Moraine can be found. At the slope underneath Alte Staffel the steepest topography of the project area is present where several cliffs of up to 30 m height and 100 m length dominate the slope (see Figure 4). These cliffs are concentrated in the eastern part of the landslide and cross the right flank of the instability reaching almost until Chatzulecher (Figure 4 and 5). In addition many paired linear depressions/ridges occur in this area, which are again sediment filled (till, glacio-fluvial sediments or recent rockfall debris) and partially act as aretic ponds.

Sector III: The lower slope sector between Aletsch Glacier, Tschifra and the plane of Kalkofen is characterized by 280 m of altitude difference and glacially abraded bedrock partially covered by till.

The ablating glacier released many uphill-facing scarps with trace length of about 100 m (40 – 360 m) not only below Kalkofen at Tschifra but also around Silbersand, where a secondary landslide at the glacier tongue location of 2015 developed in 2015 called Secondary Landslide Silbersand. The linear erosion features are shorter than in sector I and II and significantly less deep. At the plane of Kalkofen the LIA Moraine is exposed (Figure 5a,c). Gully incision of soil and bedrock slopes is primarily occurring on the foot of the slope of the last 200 m in elevation towards the glacier. The gullies are generally 10 to 20 m across and up to 10 m deep.

B Details of TPS Reflector Displacements

For the year from 2011-2012 displacement data is only existent for the undulating plain of the ridge of Moosfluh. 3D displacements are in the range of 0.06 m/a at the Sparrhorn cliffs (Refl. 5003) and 0.49 m/a at the center of the instability (Refl. 5004). Their main movement direction is NW with a tilt from 23° (Refl. 5004) up to 39° (Refl. 109) except for Refl. 5003 near Sparrhorn which is moving nearly vertically downwards. For the annual period between fall 2012 and fall 2013 3D displacements reach maximum values at reflector 5004 (0.55 m/a) and diminish along the crest towards NE to 0.43 m/a (Refl. 5005) and 0.16 m/a (Refl. 5001). Minimum values are again found at the Sparrhorn cliffs moving vertically downwards with 0.03 m/a. Azimuths of vectors vary hardly and are all in the range between 310° and 315° (towards NW) with tilts being in the range of 18° at the crest in the central part (Refl. 5004) and 30° at the other locations.

When looking at data from 2013 to 2014 additional reflectors (Refl. 28 and 29) are available which are located on the eastern flank. 3D displacements of these two reflectors are in the range of 0.04 m/a (Ref. 28) and 0.07 m/a (Ref. 29), whereas at the ridge crest reflectors displacements increase to 0.69 m/a (Ref. 5004). Azimuths of the reflectors at the eastern flank are 325-330° and differ from reflectors on the crestal plane with 315°. Tilts have a much flatter angle than in the years before and are mostly in the range of 6°-12°, except reflectors 28 (26°), 5005 (19°) and 5003 (still moving vertically downwards). For the year from 2014 to 2015 displacement data is existent for the top of the ridge (Reflectors 31, 33 & 36), a line of reflectors in the slope between the planes of Alte Staffel and Kalkofen (Reflectors 30, 32 & 35) and Reflector 34 at the slopes toe. During the monitoring period 2014/2015 maximum reflector movement is in the range of 0.8 m/a, tilts range between 10°-20° and azimuths are directed towards NW. In detail reflector 34 at the toe of the slope tilts with 14° and reflector 33 at the crest with 20°. From 2015 to 2016 3D displacement increases up to 1.45 m/a at the central crest (Refl. 36 and Refl. 5004) and decreases to 0.15 m at the eastern flank (Refl. 28 and Refl. 29). Tilts vary between minimum 15° (Refl. 32) and maximum 25° (Refl. 5005, Refl. 33, Refl. 31). Reflector 34 at the toe shows an average tilt of 17°. Movement at the Sparrhorn cliff (Refl. 5003) comes to a rest.